



HAL
open science

Ruthenium icosahedra and ultrathin platelets: the role of surface chemistry on the nanoparticle structure

Raj Kumar Ramamoorthy, Katerina Soulantica, Iker Del rosál, Raul Arenal, Philippe Decorse, Jean-Yves Piquemal, Bruno Chaudret, Romuald Poteau, Guillaume Viau

► To cite this version:

Raj Kumar Ramamoorthy, Katerina Soulantica, Iker Del rosál, Raul Arenal, Philippe Decorse, et al.. Ruthenium icosahedra and ultrathin platelets: the role of surface chemistry on the nanoparticle structure. *Chemistry of Materials*, 2022, 34 (7), pp.2931-2944. 10.1021/acs.chemmater.1c03452 . hal-03644170

HAL Id: hal-03644170

<https://hal.science/hal-03644170v1>

Submitted on 18 Apr 2022

HAL is a multi-disciplinary open access archive for the deposit and dissemination of scientific research documents, whether they are published or not. The documents may come from teaching and research institutions in France or abroad, or from public or private research centers.

L'archive ouverte pluridisciplinaire **HAL**, est destinée au dépôt et à la diffusion de documents scientifiques de niveau recherche, publiés ou non, émanant des établissements d'enseignement et de recherche français ou étrangers, des laboratoires publics ou privés.

Ruthenium icosahedra and ultrathin platelets: the role of surface chemistry on the nanoparticle structure

Raj Kumar Ramamoorthy,¹ Katerina Soulantica,^{1,*} Iker Del Rosal,¹ Raul Arenal,^{2,3} Philippe Decorse,⁴ Jean-Yves Piquemal,⁴ Bruno Chaudret,¹ Romuald Poteau,^{1,*} Guillaume Viau^{1,*}

¹ Université de Toulouse, UMR 5215 INSA, CNRS, UPS, Laboratoire de Physique et Chimie des Nano-Objets, 135 avenue de Rangueil F-31077 Toulouse cedex 4, France

² Laboratorio de microscopias avanzadas (LMA), Instituto de Nanociencia de Aragón (INA), U. Zaragoza, C/ Mariano Esquillor s/n, 50018 Zaragoza, Spain

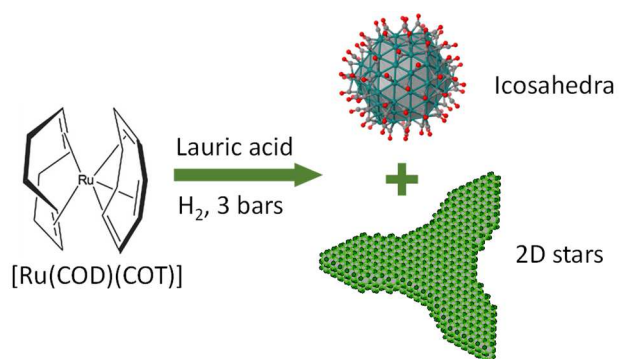
³ ARAID Foundation, 50018 Zaragoza, Spain

⁴ Université de Paris, ITODYS, CNRS, F-75006 Paris, France

Abstract

The control of the crystalline structure and shape (crystal habit) of nanoparticles (NPs) is the key to control their physical and chemical properties. Among the different metals, the crystallogenesis of ruthenium NPs has been less studied and until recently Ru-NPs crystal structure and morphology have been considered as presenting less versatility than the *fcc* metals of the platinum group. Here, we show that while the hydrogenation of [Ru(COD)(COT)] in solutions containing a long chain amine (hexadecylamine, HDA) in large excess leads to isotropic NPs adopting the expected *hcp* structure of bulk Ru, a long chain carboxylic acid (lauric acid, LA) in large excess induces the formation of Ru nano-objects of two original structures: ultrathin platelets and icosahedra. The latter have never been produced so systematically by other methods. We show that carbon monoxide, produced *in situ* by the decarbonylation of lauric acid, play a pivotal role on the stabilization of the Ru icosahedra. This result is supported by DFT calculations which show that, above a critical surface coverage of CO, small Ru icosahedra are more stable than the Ru bipyramid polyhedra crystallizing in the *hcp* structure. Thus, *in situ* production of CO results in a competition between *hcp* and icosahedral seeds, which explains the mixture of icosahedra and ultrathin platelets. Another effect of the large excess of lauric acid is the stabilization of the ruthenium precursors in solution limiting the nucleation extent and slowing down the NP growth. While the growth of the icosahedral seeds is limited because of the structural strains, the growth of the *hcp* seeds develops preferentially the (0001) facets leading to ultrathin platelets and 3-fold stars.

Table of Content Graphic



1. Introduction

During the last two decades wet-chemistry methods have accomplished considerable progress in the synthesis of metal nanoparticles (NPs) with controlled morphology, structure and surface chemistry. These NPs present a great potential for applications in the field of catalysis, which can exploit not only their high surface/volume ratio but also their structural characteristics,^{1,2,3,4,5} or in nanotechnology, which can benefit from the original properties at the nanoscale.⁶ Besides the size control of isotropic or compact polyhedral particles, which are usually generated as a result of the surface energy minimization, more complex and unusual shapes such as metal ultrathin metal nanosheets,^{7,8} nanocages,⁹ stars^{10,11,12} and highly branched particles,¹³ are targeted for their original physical properties or peculiar chemical reactivity. For instance, free-standing ultrathin metal nanosheets have recently attracted attention in the domain of catalysis as they represent an efficient strategy toward high catalytic performances and cost-efficiency, due to their ultrahigh surface area and efficient utilization of metal active sites.^{14,15} Among the metal NPs of the platinum group, as described in recent reviews,^{16,17} ruthenium NPs prepared by colloidal chemistry find a wide range of applications such as reduction or oxidation, Fischer–Tropsch synthesis and hydrogen production through amine borane dehydrogenation¹⁸ or water-splitting reactions.¹⁹ Despite all efforts to find alternative materials, ruthenium is still the best catalyst for H₂ production via ammonia decomposition.²⁰ Ruthenium NPs find also applications in electrode materials.²¹

The physical and chemical properties of colloidal metal NPs strongly depend on the NP size, shape, structural properties and electronic structure. Size-controlled ruthenium NPs have been synthesized by different methods such as the organometallic route^{22,23} or the polyol process.^{24,25,26} These methods were very useful to control the particle size of isotropic particles with very narrow size distribution. Among them, the organometallic approach for the synthesis of Ru NPs has proven to be particularly efficient in the control of the surface chemistry through ligand exchange,^{22,27} enabling high activity and selectivity in C–H activation and H–D exchange.²² The shape control of metal nanoparticles synthesized by wet-chemistry methods, particularly studied for metal NPs that crystallize in the cubic structure such as platinum,^{28,29} relies on the surface chemistry of the NPs. In the case of ruthenium, most of the reactions lead to isotropic particles that crystallize in the hexagonal close packed (*hcp*) structure.^{22,30} A recent review on Ru NPs illustrates the fact that the shape control has been less explored for Ru than for other metals.³¹

Only a few methods producing anisotropic Ru NPs have been described so far. Hour-glass like NPs were obtained by reduction of ruthenium(II) acetylacetonate in oleylamine.³² Ultrathin triangular platelets and capped-columns were synthesized by reduction of RuCl₃·xH₂O under hydrothermal conditions in solutions of formaldehyde containing PVP and/or sodium oxalate in various concentrations.³³ Ultrathin *hcp* Ru nanosheets were obtained by a solvothermal method in the presence of isopropanol and urea.¹⁹ Branched ruthenium particles were obtained by decomposition of Ru₃(CO)₁₂ in toluene at 160 °C under hydrogen atmosphere in the presence of a mixture of hexadecylamine and hexadecanoic acid.³⁴ In addition, syntheses by wet-chemistry of Ru NPs that do not crystallize in the thermodynamically stable *hcp* structure are very scarce. Recently, Ru NPs with a face centered cubic (*fcc*) structure were produced by chemical reduction of [Ru(acac)₃] in solution.^{26,35,36} The Ru *fcc* structure was studied by conventional X-Ray Diffraction (XRD) and high-energy XRD and Pair Distribution Function (PDF) analysis.^{37,38} Branched Ru particles crystallizing as a mixture of *fcc* and *hcp* phases were obtained by reducing Ru(III) precursors with metal carbonyls at high temperature.¹⁸ Another approach to synthesize Ru nanostructures with the *fcc* structure is the seed mediated growth method developed by Xia and co-workers. Ru nanocages with icosahedral shape and *fcc* structure were obtained by growing a thin Ru shell on Pd icosahedral particles, followed by the selective chemical etching of the Pd core.⁹ Following the same approach Ru octahedral particles crystallizing with the *fcc* structure were obtained using rhodium cubes as seeds.³⁹ Epitaxy effects were also evidenced in more classical heterogeneous catalyst routes. Ru nanoparticles supported on carbon nitride C₃N₄ prepared at high temperature exhibited *fcc* and *hcp* structures or mixtures of both.⁴⁰ The role of the carbon nitride on the stabilization of the *fcc* phase was supported by Density Functional Theory (DFT) calculations.

Several examples showed that in some cases the catalytic activities of Ru NPs can be greatly enhanced by the *fcc* structure or by a disordered structure resulting of mixtures of *fcc* and *hcp* phases on the same particles.^{26,21,35,39,40} However, a general description of the stabilization of the *fcc* phase in non-supported/free-standing Ru NPs prepared by colloidal chemistry is still lacking. At very small size, Ru clusters can adopt atomic structures very different from the bulk. Electron- and atom-precise medium-sized Ru clusters, bare⁴¹ or stabilized with hydrides,⁴² have been generated in gas-phase by magnetron sputtering. Their structure has been elucidated by a combination of trapped ion electron diffraction (TIED), genetic algorithms coupled with determined empiric potentials and DFT calculations. For example, the electron scattering signal of Ru₅₅⁻, 55 being a magic number for closed-shell icosahedra and cuboctahedra, is consistent with a close-packed structure resembling segments of the *hcp* bulk.⁴¹ Interestingly, while the structure of the Ru₁₉⁻ cluster is consistent with a closed-shell octahedral geometry, it exhibits a bi-icosahedral structure upon hydrogenation, the driving force being the higher hydrogen adsorption energies on that metal core.⁴³ For bigger particles (Ru_n clusters with n > 55), Soini et al. predicted that the *hcp* structure is more stable than the *fcc* one.⁴⁴ In addition, DFT calculations were performed on bare Ru NPs with different structures containing up to 1500 atoms.⁴⁵ The best candidate to compete with *hcp* Ru nanocrystals is the icosahedral Ru, but despite their high coordination numbers and stabilizing twin boundaries, the icosahedral Ru NPs were always found thermodynamically less stable than the *hcp* Ru nanocrystals of the same size and up to now no systematic strategy has been defined for the synthesis of Ru icosahedra .

In this paper, we investigate the Ru NPs synthesis by the organometallic approach, using as stabilizing agents a long chain carboxylic acid and a long chain primary amine in large excess relatively to the Ru precursor concentration. We show that the shape and structure of the Ru NPs prepared by decomposition of [Ru(COD)(COT)] (COD = cyclooctadiene, COT = cyclooctatriene) depend critically on the relative concentration of the acid and the amine. Large amounts of lauric acid favor the formation of Ru icosahedral particles together with *hcp* Ru ultrathin platelets and three-fold nano-stars. Surface characterization shows that in these cases carbon monoxide, generated *in situ* by decomposition of the carboxylic acid ligands, is adsorbed on the particle surface. On the other hand, ultrasmall NPs with the *hcp* structure were observed in presence of large concentration of amine and adsorbed N atoms were observed at the surface of Ru NP. In order to understand the role of carbon monoxide on the control of the Ru NP structure, first principles thermodynamic calculations of the total energy of Ru NPs containing 147 atoms with different shapes and structures were calculated as a function of temperature and partial pressure of CO.

2. Experimental

2.1 Materials and methods

All syntheses have been performed under inert conditions, either in an Ar filled glove-box or by using standard Schlenk techniques. All chemicals, [Ru(COD)(COT)] (furnished by NANOMEPS), lauric acid (Acros, 99%) and hexadecylamine (Sigma Aldrich, 98%) were kept in the glove-box and used without further purification. Freshly dried and degassed 1,3,5-trimethylbenzene (mesitylene) and pentane were also kept in the glove-box.

2.2 Ru Nanoparticle synthesis

Ru nanoparticles were synthesized by hydrogenation of the organometallic precursor [Ru(COD)(COT)]. In the glove-box, 0.05 M of [Ru(COD)(COT)] was added to 10 ml of 1,3,5-trimethylbenzene containing lauric acid (LA) and hexadecylamine (HDA) at different concentrations in the range 0.05 M - 0.40 M for the acid and 0 M - 0.40 M for the amine, and placed into Fischer-Porter bottles. All resulting mixtures

were yellow irrespectively of the molar concentrations of amine and acid. The sealed Fischer-Porter bottles were connected to a vacuum-line for evacuating Ar and filling with H₂ to 3 bar. After pressurizing the Fischer-Porter bottles, the solutions were introduced into a pre-heated oil bath at 150 °C and let to react under stirring for 96 h. After completion of the reaction, the final brown colored Ru nanoparticles suspensions were cooled to room temperature and after evacuating the H₂, they were stored under the inert atmosphere of the glove box.

2.3 Characterization

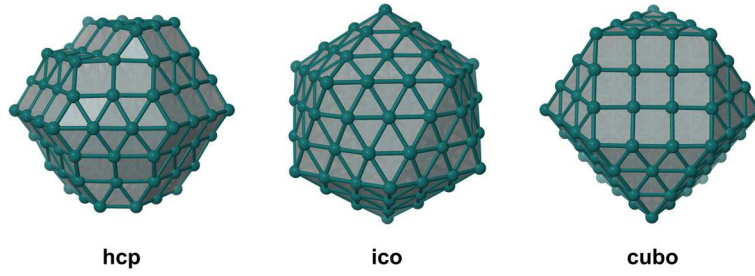
Transmission electron microscopy observations were performed on a JEOL JEM 1400 microscope operating at 120 kV. Scanning transmission electron microscopy coupled with a bright field detector and a high angle annular dark field imaging (HAADF-STEM) was performed on a probe corrected JEOL JEM-ARM200F instrument equipped with a cold field emission gun. Electron tomography of ruthenium stars were done with a FEI Titan electron microscope operating at 300 kV. In all cases the particles were diluted 10 times, one drop of the suspension was deposited on a carbon coated copper grid and the solvent was evaporated at room temperature under vacuum.

Infrared spectra FT-IR spectra were recorded on a nitrogen purged Nicolet 6700 FT-IR spectrometer in the range 4000-700 cm⁻¹, using a Smart Orbit ATR platform. The mother suspensions were ultracentrifuged using a Sorvall MTX150 equipment and dispersed in pentane after removing the supernatant. Few drops of the colloidal suspensions were deposited on a Ge wafer and the spectrum was recorded when the solvent was fully evaporated.

X-ray photoelectron spectroscopy (XPS) spectra were recorded using a K-Alpha+ system (ThermoFisher Scientific, East-Grinstead, UK) fitted with a micro-focused and monochromatic Al K α X-ray source (1486.6 eV, spot size of 400 μ m). The spectrometer pass energy was set to 150 and 40 eV for the survey and the narrow high-resolution regions, respectively. The chemical composition was determined by using the manufacturer sensitivity factors with Avantage software, version 5.9902. The spectra were calibrated with the (C-C/C-H) C1s component due to the use of the charge compensation system for insulating samples analysis. Few drops of the colloidal suspensions were deposited on Si wafers, the spectrum was recorded when the solvent was fully evaporated.

2.4 Theoretical calculations

DFT calculations were done with the Vienna ab initio simulation package, VASP,^{46,47} by using the exchange-correlation potential approximated by the generalized gradient approach proposed by Perdew, Burke, and Ernzerhof (PBE).⁴⁸ The method uses the plane-augmented wave scheme^{49,50} to treat core electrons, with a kinetic energy cutoff of 500 eV.^{51,52} The 2s and 2p orbitals of carbon and oxygen and 4p, 4d and 5s orbitals of ruthenium have been treated explicitly in the valence. Γ -centered calculations⁵³ were performed with a Gaussian smearing (σ) of 0.02 eV, energies being therefore extrapolated to $\sigma = 0.00$ eV. All atoms were allowed to relax with a force convergence threshold defined as 0.02 eV/Å. The supercell size was set up so as to ensure a vacuum space of *ca.* 12 Å between periodic images of metal clusters, *i.e.* 31 x 31.5 x 32 Å³. The d-band center⁵⁴ values were calculated after projection by the Lobster software⁵⁵ of the planewave/pseudopotential wavefunction on a local Slater atomic basis set.



Scheme 1. Models of 147-atoms Ru NPs considered in this study, *hcp* truncated bipyramid, icosahedron and *fcc*-cuboctahedron.

Three ~1.4 nm polyhedra, *hcp* bipyramid, icosahedron (*ico*) and *fcc* cuboctahedron (*cubo*), have been considered in this study, see Scheme 1. They are all composed of 147 atoms, a magic number both for McKay icosahedra and cuboctahedra.⁵⁶ The *hcp* cluster of 147 atoms that have been chosen is very similar to the one described by Nørskov and co-workers following a Wulf construction.⁵⁷ Because they are only slightly smaller than the observed Ru NPs, the calculated energy trends are expected to be transferable to the experimental case. Their atomic coordinates were automatically generated with the polyhedra software developed in the group.⁵⁸ A line of atoms has been removed between the (001) and (101) planes in the *hcp* bipyramid, thus yielding a 147-atoms cluster that exhibits the so-called B5 sites.⁵⁷ Thanks to a Monte-Carlo based tool, CO ligands in $Ru_{147}(CO)_n$ clusters were randomly grafted on the surface by minimizing their mutual interaction.⁵⁸ The resulting geometries were then optimized at the DFT-PBE level of theory. Each of the three considered metal cores were stabilized by *ca.* $\theta = 0.25, 0.75, 1.00$ and 1.5 CO per surface Ru atom (Ru_{surf}). Adsorption free energies $\Delta G_{ads}(T, p_{CO})$ were calculated under realistic temperature (T) and CO pressure (p_{CO}) with the *ab initio* thermodynamics method,⁵⁹ recently successfully applied to the theoretical determination of the surface composition of Ru NPs in equilibrium with a mixture of compounds (namely H_2/CO and $H_2/MeCOOH$).^{51,52} The chemical potential for CO(g) is the same as the one used in Ref. [51]. To be more explicit, in the present study ΔG_{ads} is calculated for the equilibrium reaction:



Cohesive energies per atom are calculated as:

$$E_{coh} = \frac{E_N - NE_1}{N}$$

where E_N is the total energy of a N -atoms Ru NP and E_1 is the energy of a single Ru atom.

The surface energy γ can be calculated using the cohesive energy per atom in the bulk state, $E_{coh,b}$:

$$\gamma = \frac{E_N - N(E_{coh,b} + E_1)}{S}$$

where S is the surface area of the NP. $E_{coh,b}$ was calculated to be -6.67 eV, a value close to experiments, -6.74 eV.⁶⁰

Adsorption energies per ligand L , $E_{ads/N}$, can be calculated as a first indication of the adsorption strength, by directly using DFT energies: $E_{ads/N} = (E_N - E_{NP} - N \cdot E_L)/N$.

3. Results and Discussion

3.1 Morphology and structure

The syntheses of Ru NPs were carried out by hydrogenation of [Ru(COD)(COT)] in 1,3,5-trimethylbenzene containing different concentrations of LA and HDA. Both molar ratios $A = [\text{LA}]/[\text{Ru}]$ and $B = [\text{HDA}]/[\text{Ru}]$ were independently varied, from 0 to 8. The particle size, shape and structure were found to depend on both ratios. The particle morphologies are summarized in Table S1 of supplementary materials. The mean particle size (d_m) and the standard deviation of the size distribution (σ) obtained for different values of A and B are given in Table S2 (supplementary materials).

In the absence of LA ($A = 0$) and with a large excess of HDA ($B = 8$), isotropic NPs with a mean diameter of 2 nm were obtained (Fig. 1a). Under the same conditions but with lower amount of HDA ($B < 4$), the particles were found agglomerated forming chains (Fig. S1 in supplementary materials) in agreement with previous observations.²²

In the absence of amine ($B = 0$), mixtures of small isotropic NPs, triangles and three-fold stars were observed, with about 50% in number for the isotropic NPs (Fig.1b and Fig. S2 in supplementary materials). With a large excess of acid ($A = 8$) the population of triangles decreased in favor of the three-fold stars. In addition, the mean size of the three-fold stars increased from 8 nm to 12 nm when the ratio A was increased from 2 to 8. The mean sizes of the isotropic particles were 2.2 and 3.5 nm for the molar ratio A of 2 and 8, respectively. It is interesting to note that, unlike the HDA, small amounts of LA are sufficient to stabilize small Ru NPs. We observed also that the mean particle size increased with higher LA concentration. This can be explained by the stabilization of the Ru precursor in solution, when the LA concentration is increased, which results in lowering the nucleation extent. It has been shown that carboxylic acids react with [Ru(COD)(COT)] and depending on the ratio between the acid and [Ru(COD)(COT)], complexes comprising carboxylate ligands in different coordination modes.⁶¹ These complexes are less reactive than the raw [Ru(COD)(COT)] precursor.

In the presence of a mixture of LA and HDA, the particle morphology was found to depend mainly on the ratio A/B and to a less degree on the total concentration of LA and HDA.

Isotropic NPs with very small mean diameter ($d_m \leq 2$ nm) were found when the ratio A was limited to 1 and B was at least equal to A ($A = 1$ and $B \geq A$). Representative TEM images for $A = 1$ and $B = 1, 4, 8$, are shown in the supplementary materials (Fig. S3 in supplementary materials). In these conditions the Ru NPs are very similar to the ones prepared in the absence of LA.

When LA was added in sufficient amount ($A \geq 2$) and when the HDA concentration did not exceed that of LA ($A \geq B > 0$), mixtures of faceted NPs (triangles, truncated triangles or hexagons) and isotropic NPs were observed. In Figure 1c is shown a TEM image of Ru NPs prepared in equimolar mixture of LA and HDA ($A = B = 4$). In this case, the mean sizes of the faceted and small isotropic particles were of 3.7 and 1.8 nm, respectively. Additional representative TEM images of samples prepared with $A \geq 2$ and $A \geq B > 0$ are given in the supplementary materials (Fig. S4a-b). All these images show a polymorphism as in the samples prepared in the absence of HDA, however, with a smaller relative number of isotropic NPs (between 10 and 35 % compared to 50 % in the absence of HDA). For the samples prepared in large excess of LA, the particle size increased when the LA concentration was increased. The triangle prepared with $A = 4$ and $B = 1$ exhibited a mean size of 4.2 nm, smaller than the triangle prepared with $A = 8$ and $B = 2$, that exhibited a mean size of 7 nm (Fig. S4 and Table S2). As mentioned above, an increasing amount of LA can reduce the nucleation extent because of the formation of stable intermediate Ru carboxylates which participate mainly to the growth. On the other hand, the effect of

the LA concentration on the isotropic particles mean size was less pronounced, their mean size was always in the range 1.8 - 2.5 nm whatever A and B. Interestingly, when LA and HDA were both added in large excess (A = B = 8) the mean particle size decreased compared to the sample A = B = 4, showing that a large excess of HDA may favor the nucleation. For A = B = 8, the two types of NPs are hardly distinguished on the conventional TEM (Fig. S4c) but are revealed by the high-resolution images (see next section).

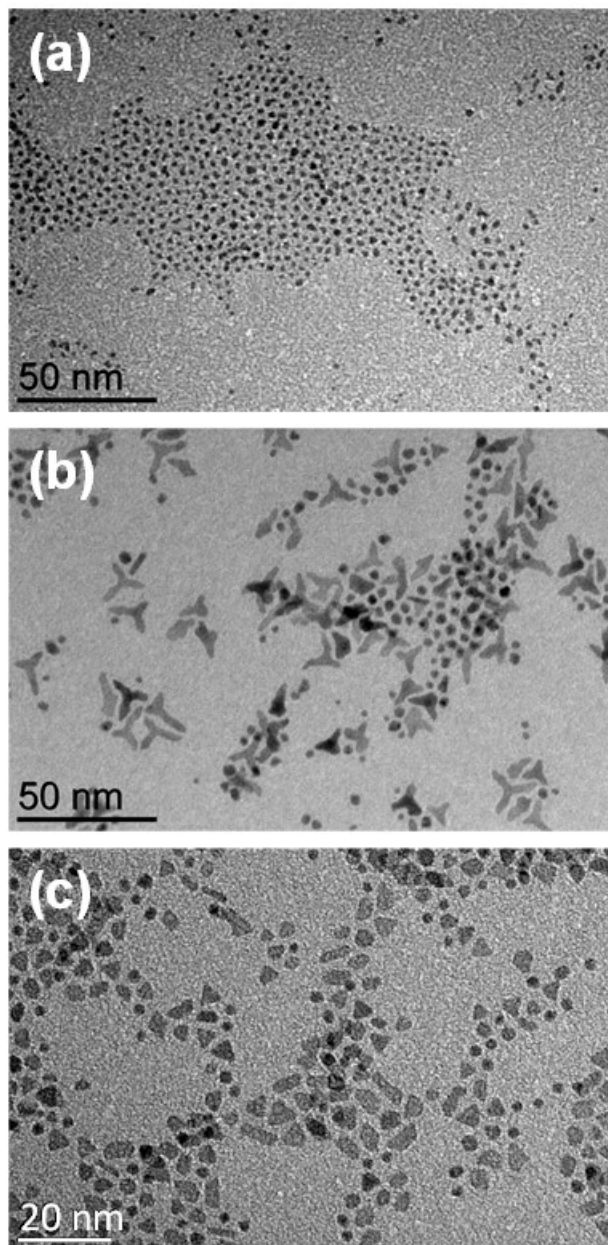


Figure 1. Transmission electron microscopy images of ruthenium nanoparticles prepared by hydrogenation of 0.05M of [Ru(COD)(COT)] in solution of 1,3,5-trimethylbenzene containing LA and HDA with different the molar ratio $A = [\text{LA}]/[\text{Ru}]$ and $B = [\text{HDA}]/[\text{Ru}]$: (a) $A = 0, B = 8$; (b) $A = 8, B = 0$; (c) $A = B = 4$.

The low contrast of the star-like and triangular nano-objects indicates that they have a small thickness. The atomic structure of the particles was analysed using scanning transmission electron microscopy using a probe corrected microscope. The different types of samples, isotropic NPs only, mixture of faceted and isotropic NPs and mixtures of three-fold stars or triangles and isotropic NPs depending on the A and B values, and the structure of the different particles are summarized in Figure 2.

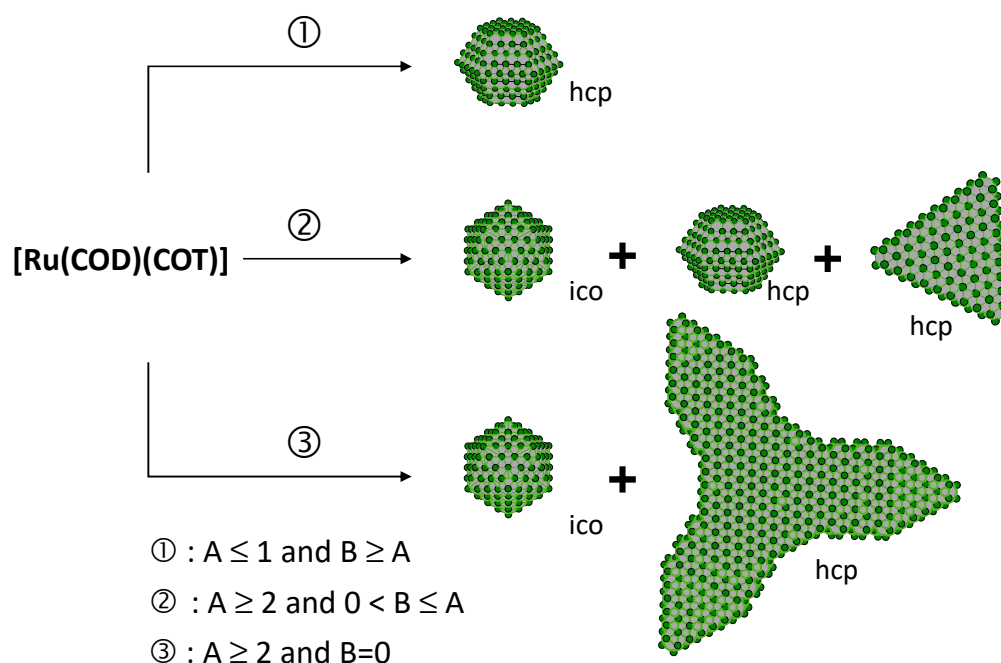


Figure 2. Summary of shape and structure of Ru NPs prepared by hydrogenation of $[\text{Ru}(\text{COD})(\text{COT})]$ with different ratios $A = [\text{LA}]/[\text{Ru}]$ and $B = [\text{HDA}]/[\text{Ru}]$. Information about the mean size and relative amount of each populations are given in Table S2 (Supplementary information).

High-resolution HAADF STEM characterizations were carried on the faceted NPs and stars obtained in the absence of HDA or in large excess of LA and demonstrated that these are indeed, 2D nano-objects. Most of the triangular platelets and the three-fold stars adopt a flat orientation on the TEM grids. A representative high-resolution HAADF-STEM image of Ru triangular platelets prepared with an excess of acid ($A = 4$, $B = 1$) is presented on Figure 3. The particles crystallize in the *hcp* structure and are oriented in $[0001]$ zone axis, which means that the crystallographic *c* axis is perpendicular to the platelet plane. The edges of the triangular platelets correspond to the $\{10\bar{1}0\}$ crystallographic planes (Fig. 3). The three-fold stars prepared in the absence of HDA crystallize also with the *hcp* structure with the $[0001]$ axis perpendicular to the star plane, as shown in the example given in Figure 4. The core of the stars is similar to the triangle described above, but the edges of the arms are no longer $\{10\bar{1}0\}$ planes but $\{2\bar{1}\bar{1}0\}$ planes, therefore different from the edges of the initial triangle (Fig. 4). Some stars and platelets were deposited edgewise on the TEM grids giving the opportunity to measure precisely their thickness. In most of the cases, the platelets are composed of only 5- or 6-atomic layers, corresponding respectively to 2 and 2.5 unit cells along the crystallographic axis *c* (Fig. 4b and Fig. S5 in supplementary materials). The homogeneity of the thickness is noticeable showing that the growth of the basal planes is highly favored over the growth along the *c* axis. The thickness of the 5-atomic layer platelets was comprised between 8.6 Å, i.e. the expected value for 2 unit cells along *c*, and 8.9 Å

corresponding to a dilatation of 4 % of the unit cell. The thickness of the 6-atomic layer platelets was found very close to 10.7 Å, the expected value for 2.5 times the c value. Thus, in large excess of LA, the (0001) planes of the hcp Ru are strongly stabilized by the long chain carboxylates (see next section) preventing the incorporation of Ru atoms perpendicularly to the basal planes. Triangular and hexagonal platelets result from a preferential growth of the (0001) plane with lateral $\{10\bar{1}0\}$ facets. The stars arise from a two-step growth. Triangular or hexagonal platelets are formed first and at a given point of the reaction, the growth still develops the (0001) plane but with $\{2\bar{1}\bar{1}0\}$ edges, due to a stronger stabilization of the $\{10\bar{1}0\}$ facets and a higher growth rate of the $\{2\bar{1}\bar{1}0\}$ facets. Therefore, the 2D stars result from a subtle balance between the growth rates of the $\{10\bar{1}0\}$ and $\{2\bar{1}\bar{1}0\}$ lateral edges.

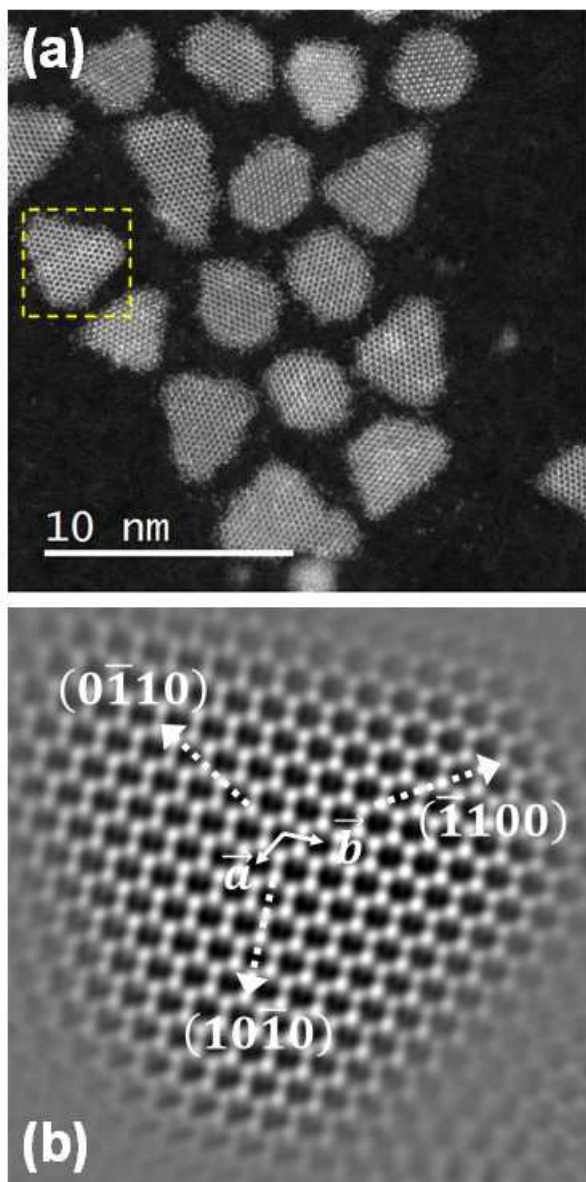


Figure 3. (a) High resolution HAADF-STEM image of Ru nanoplatelets prepared with molar ratio $A = [LA]/[Ru] = 4$ and $B = [HDA]/[Ru] = 1$; (b) Fourier filtered image of the framed nano-triangle showing an orientation in $[0001]$ zone axis, the expected atomic pattern with 2 atoms per unit cell and the crystallographic indexes $\{10\bar{1}0\}$ of the edges.

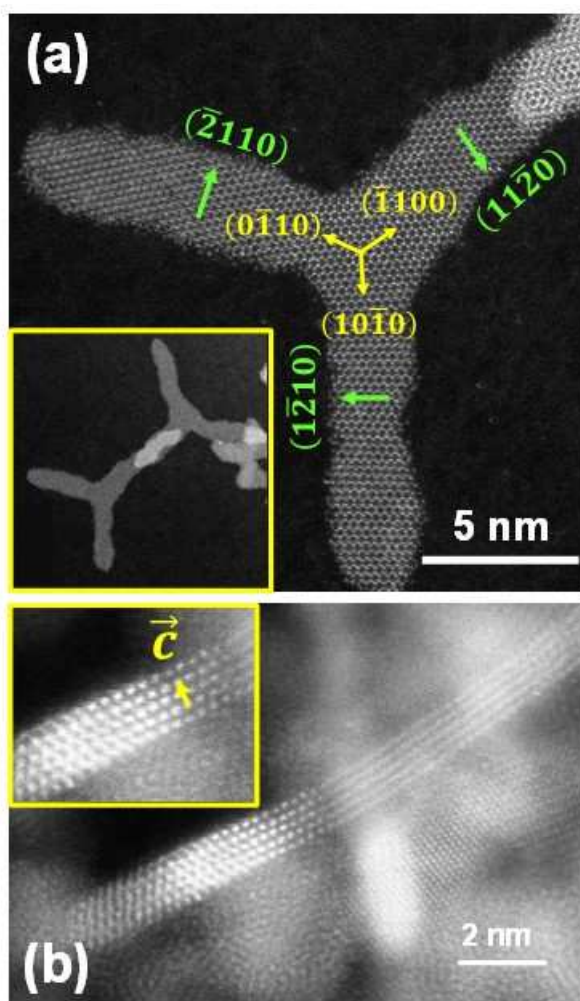


Figure 4. (a) High resolution HAADF-STEM image of a Ru three-fold star prepared with molar ratio $A = [LA]/[Ru] = 8$ and $B = [HDA]/[Ru] = 0$. *Inset*: image at lower magnification showing two three-fold stars with two branches overlapped; (b) High-resolution HAADF-STEM edgewise images Ru nanoplatelets revealing a stacking of five (0002) Ru layers with a thickness comprised between 8.6 and 8.9 Å (the left part of the platelet is oriented in the $[11\bar{2}0]$ zone axis, the c axis is perpendicular to the layers).

The isotropic NPs that are present with the triangle, faceted and star-shaped NPs were also characterized by high-resolution HAADF-STEM. The observations revealed that isotropic NPs of icosahedral structure crystallized together with the particles of *hcp* structure. A representative image of Ru NPs prepared with large excess of LA and HDA in equimolar proportion ($A = B = 8$) is given on the Figure 5, showing on the same area an icosahedron viewed along a five-fold axis (yellow circle), a particle crystallizing with the *hcp* structure and oriented in the $[0001]$ zone axis (red circle), and a platelet oriented edgewise (green rectangle). For the *hcp* particle, the $\{10\bar{1}0\}$ reticular distances of 2.38 Å measured from the FFT are very close to the distance of 2.343 Å in bulk Ru. The FFT of the icosahedron exhibits the ten equidistant spots resulting from the Moiré pattern generated by the overlapping of several atomic layers of an *fcc* stacking in $[110]$ zone axis, characteristic of multiply twinned particles. The ten spots correspond to $\{11\bar{1}\}$ reflections of the *fcc* structure. The average $\{111\}$ distance calculated from the FFT was found of 2.29 Å. This value is slightly higher than the distances of

2.23-2.26 Å reported for Ru *fcc* NPs with different sizes,^{37,38} but remaining below the limit of 5 % of uncertainty of the STEM technique.

As mentioned in the introduction, most of the Ru particles prepared by chemical routes crystallize in the *hcp* structure. Some rare examples of Ru particles of *fcc* structure were reported and even rarer are the examples of Ru multiply twinned particles. Only two examples characterized by high-resolution TEM studies were found in the literature. Kusada et al. reported five-fold decahedral Ru NPs³⁵ and Alyami et al. identified some icosahedra among Ru NPs prepared at high temperature and high pressure.¹⁸ In order to pinpoint the crucial parameters allowing the formation of Ru icosahedra by the organometallic route, structural studies were systematically carried out on various samples prepared with different ratios A and B.

Interestingly, no particles with icosahedral structure were found in the samples prepared in the absence of LA (A = 0, B = 8) or with A = B = 1 (case 1 of Fig. 2). In these cases, only *hcp* particles were found on the HAADF-STEM images. All the particles were indexed as *hcp* particles oriented along the $[11\bar{2}0]$ or along the $[0001]$ zone axis (Fig. S6, supplementary materials). On the other hand, icosahedral particles were detected in all samples prepared with LA provided it was present in sufficient concentration (case 2 of Fig. 2). Moreover, in the absence of HDA (B=0) or in large excess of LA, only icosahedral particles were detected in the population of small isotropic NPs (case 3 of Fig. 2). Examples of high-resolution HAADF-STEM images of such NPs, prepared in the absence of HDA (B = 0) and of those prepared with an excess of lauric acid (A = 8 and B = 2), are shown in Figure 6. Icosahedra viewed along five-, three- and two-fold axes were clearly identified. The experimental images are very similar to the projection of a model Ru icosahedron built with 309 atoms and of size 2.1 nm (see also Fig. S7, supplementary materials). The chemical composition of the icosahedral particles was verified by local energy dispersive spectroscopy (EDS) analysis in order to exclude any possibility of impurities present in the nanoparticles and inducing the formation of an icosahedral phase. Spectra of several isolated icosahedra showed that they contained only ruthenium and were free of impurities of other metals (Fig. S8, supplementary materials).

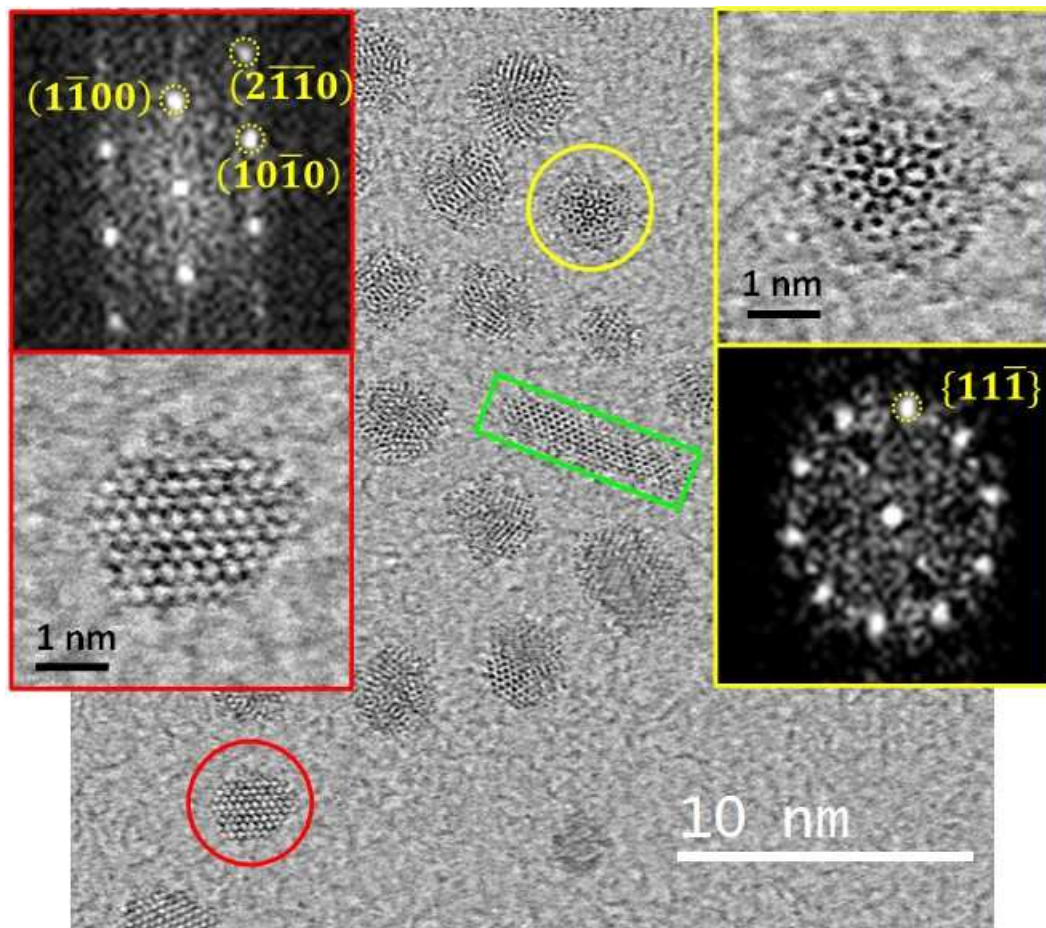


Figure 5. High resolution HAADF-STEM image of Ru nanoparticles prepared with $A = B = 8$ showing particles with different structure. Inset on the left: zoom image and calculated FFT of a particle crystallizing in the *hcp* structure and oriented in the $[0001]$ zone axis; Inset on the right: zoom image and calculated FFT of particle with an icosahedral structure viewed along a five-fold axis, the FFT exhibits the ten equidistant spots characteristic of the Moiré pattern generated by the overlapping of several atomic layers in $[110]$ zone axis. The spots visible on the FFT correspond to $\{11\bar{1}\}$ reflections.

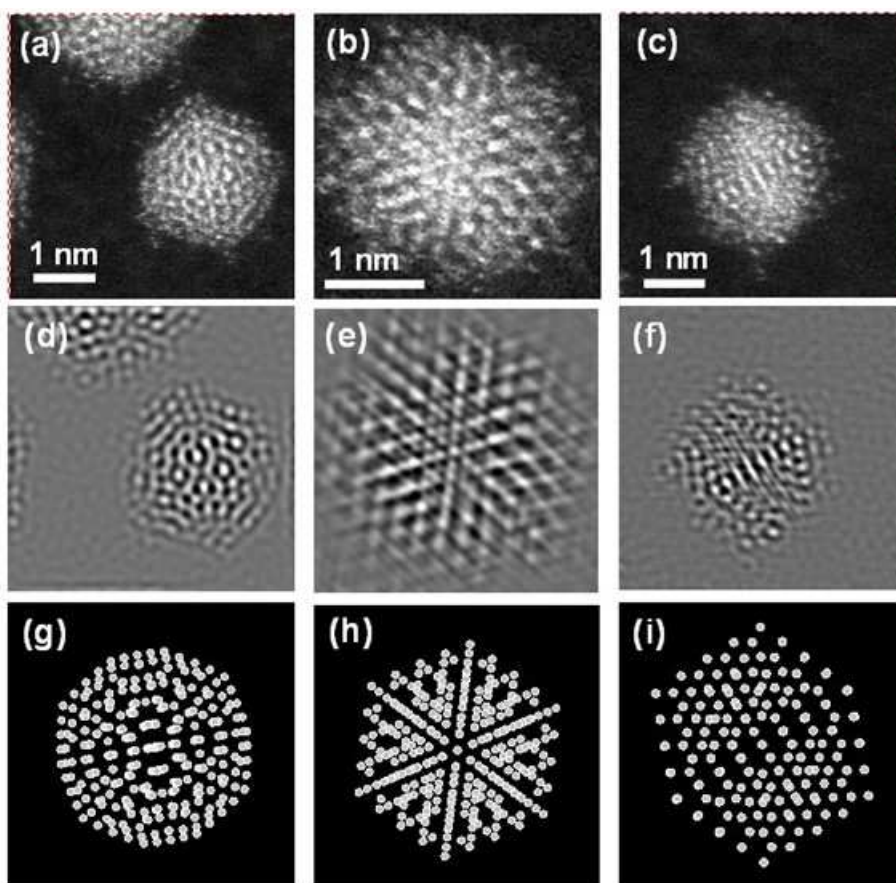


Figure 6. (a-c) High resolution HAADF-STEM images of a Ru nanoparticles with icosahedral structure; (d-f) Corresponding Fourier filtered images; (g-i) Model of a 309 atoms Ru icosahedron viewed along an axis tilted of 3° with respect to a five-fold axis (g), a three-fold axis (h) and a two-fold axis (i).

3.2 Surface chemistry

The stabilization of the icosahedral structure for very small metal particles is generally attributed to a minimization of the surface energy by exposing only close-packed facets at the expense of the energy of the core that increases because of structural distortion. Here two structures have been evidenced for particles that present almost the same size. In order to investigate the relationship between the surface chemistry and the particle structure, FT-IR and XPS spectra of Ru NPs prepared under different conditions were recorded.

Figure 7 shows FT-IR spectra of Ru particles prepared with various A and B ratios. The FT-IR spectra of the particles prepared in the absence of HDA ($B = 0$) exhibit a small peak at 2047 cm^{-1} attributed to the vibrational frequency of carbon monoxide adsorbed “on-top” at the Ru NP surface (terminal CO) and a broader band centered around $1970 - 1980\text{ cm}^{-1}$ corresponding to the vibrational frequency of bridging CO molecules.⁶² As no CO was introduced in the reactor, this is a clear evidence that CO was produced *in situ* during the reaction and remained adsorbed at the particle surface. The unique source of CO in the reaction medium is lauric acid, the decomposition of which is likely catalyzed at high temperature by ruthenium complexes or clusters.⁶¹ The other features of the FT-IR spectrum of the

particles prepared with $A = 2$ and $B = 0$ (Fig. 7a) are the $\nu(\text{CH})$ in the region $2850\text{--}2950\text{ cm}^{-1}$ and the $\delta(\text{CH})$ around 1415 cm^{-1} showing the presence of long alkyl chains. The band corresponding to the stretching vibration $\nu(\text{C=O})$ of lauric acid are not seen. Bands of weak intensity that could correspond to the symmetric and asymmetric $\nu(\text{CO})$ of the carboxylate ions are observed on both sides of the $\delta(\text{CH})$ band.⁶³ On the other hand, the band at 1700 cm^{-1} corresponding to $\nu(\text{C=O})$ of lauric acid is clearly seen on the spectrum of the sample prepared with a large excess of lauric acid ($A = 8$, $B = 0$) (Fig. 7a). The peak position is the same as in the pure lauric acid spectrum showing that the main part of the acid is free (not strongly bound to the Ru particle surface), thus that was not completely eliminated during washing procedure. The ligands present on the surface of the particles prepared with pure LA, are thus a mixture of CO and long chain carboxylates ions, the last ones being in small amount.

The bands of the carbon monoxide and $\nu(\text{C=O})$ of lauric acid are still visible on the FT-IR spectrum of the sample prepared with $A = 8$ and $B = 2$, however with weaker intensities than in the spectrum of the particles prepared in the absence of amine. Moreover, two additional peaks are observed that were absent of the spectrum of the particles prepared with $B = 0$, a peak at 1640 cm^{-1} and a peak at 3313 cm^{-1} attributed, respectively, to the stretching vibration $\nu(\text{C=O})$ and to the stretching vibration $\nu(\text{N-H})$ of an amide group.⁶⁴ This shows that the hexadecylamine reacted with lauric acid to form N-hexadecyl laurylamide that remains adsorbed at the Ru NPs surface. It has been shown that this reaction also takes place during the formation of Co nanorods in the presence of LA and HDA.⁶⁵ The formation of N-hexadecyl laurylamide was confirmed by the FT-IR spectrum of the particles prepared with an equimolar mixture of LA and HDA ($A = B = 8$) with more intense peaks at 3313 cm^{-1} and 1640 cm^{-1} . The absence of peak at 1700 cm^{-1} shows that the lauric acid is no more present at the end of the reaction (Fig. 7a). The absence of the CO peaks shows also that, in the presence of HDA, the decarbonylation of the LA is in competition with the amide formation. As expected, in the absence of LA the FT-IR spectrum of the *hcp*-Ru NPs does not exhibit the CO features which confirms that CO comes from the decarbonylation of the lauric acid (Fig. 7a). The FT-IR spectra show a very good correlation between the relative number of icosahedral particles and the intensity of the CO bands. In the absence of HDA, the CO bands are intense and as mentioned above all the small particles exhibit an icosahedral structure. With $A = 8$ and $B = 2$ the CO band is weaker and the number of small isotropic particles is less, mixture of isotropic particles and presence of small isotropic particles with the *hcp* structure (Fig. 2). In the absence of LA, CO cannot be produced in the medium, the small isotropic particles exhibited only the *hcp* structure. With $A = B = 4$ (Fig. 1c), the CO band is absent of the FT-IR spectrum which can be due to a small number of icosahedral NPs, but the count of the relative numbers of icosahedra and *hcp* particles is more difficult on the conventional TEM images because both type of particles present the same shape and almost the same size. We can finally note the absence of peaks between 3000 and 3100 cm^{-1} , i.e. in the region of the stretching vibrations $\nu(\text{C-H})$ of aromatic rings showing that the trimethylbenzene is always removed with the washing procedure.

The XPS survey scans of the particles prepared in the presence of HDA exhibited the Ru 3d, Ru 3p, C 1s and N 1s peaks. In the region $280\text{--}290\text{ eV}$, the overlapping of the C 1s and the Ru $3d_{3/2}$ peaks makes difficult an accurate analysis of the high-resolution XPS spectra. Nevertheless, for all the samples analyzed, whatever the ratio A and B, the main contribution of the Ru $3d_{5/2}$ peak appears at 280.1 eV , which is consistent with Ru in the zerovalent state (Fig. S9, supplementary materials).⁶⁶ The N 1s high-resolution spectrum of the particles prepared in the absence of LA ($B = 8$) exhibited two main peaks centered at 399 eV and 397.5 eV and a minor one centered at 401.3 eV (Fig. 8a). The peaks at 399 eV and 401.3 eV correspond to N atoms of hexadecylamine and hexadecylammonium ions, respectively.⁶⁷ The peak at low energy corresponds to N atoms adsorbed on the surface⁶⁸ of the Ru NPs and/or to a surface nitridation of the Ru NPs.⁶⁹ It shows a partial decomposition of the HDA, resulting from the C-N activation, likely catalyzed by the Ru nanoparticles in presence of molecular hydrogen. Ruthenium is

known to be a good hydrodenitrogenation catalyst.⁷⁰ The possibility to form surface nitride has recently been demonstrated upon reacting the surface of Ru NPs with NH_3 .⁷¹ The N 1s high-resolution spectrum of the particles prepared with HDA and an excess of LA (A=8, B=2) exhibited a main contribution centered at 399.8 eV attributed to N atoms of N-hexadecyl laurylamide, in agreement with the FT-IR spectroscopy. Three additional contributions centered at 397.5 eV, 399 eV and 401.1 eV, corresponding to the N atoms of Ru nitride, amine and ammonium groups, respectively, are also observed (Fig. 8b). After several washings, the N 1s XPS spectrum did not exhibit the peak at 399.8 eV anymore, but only the three contributions centered at 397.5 eV, 399.3 eV and 401.2 eV (Fig. 8c), showing that the amide is weakly adsorbed at the Ru NP surface. The peak at 397.5 eV confirms that a partial decomposition of the HDA to form Ru nitride occurs, which is however in competition with the formation of the amide in the presence of LA. It is interesting to note that the HDA was not completely converted into the amide despite the large excess of LA since the signal at 399 eV is still visible.

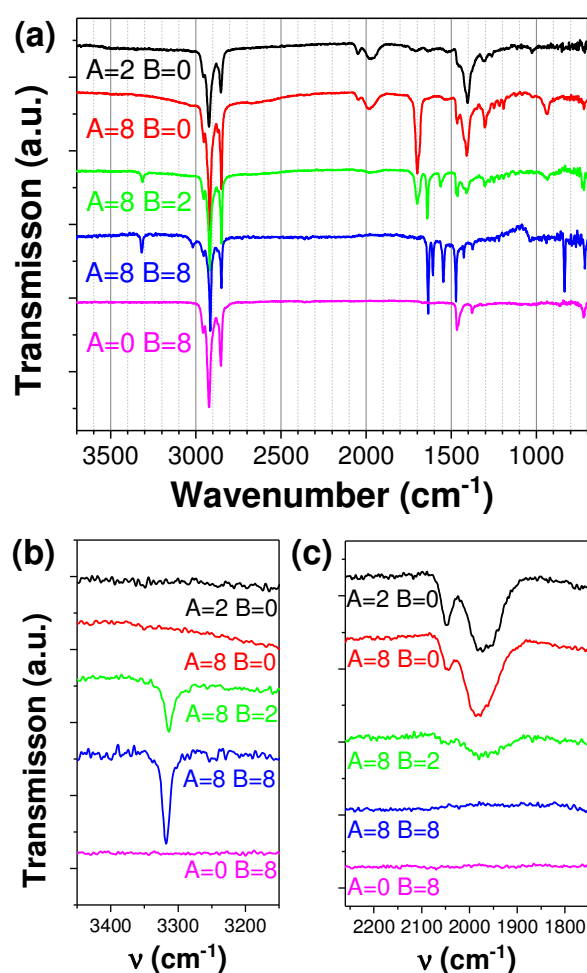


Figure 7. FT-IR spectra of Ru nanoparticles prepared by hydrogenation of $[\text{Ru}(\text{COD})(\text{COT})]$ in a solution of 1,3,5-trimethylbenzene containing LA and HDA with various molar ratio $A = [\text{LA}]/[\text{Ru}]$ and $B = [\text{HDA}]/[\text{Ru}]$: (a) full spectra ; (b) zoom on the $\nu(\text{N-H})$ region ; (c) zoom on the $\nu(\text{C=O})$ region.

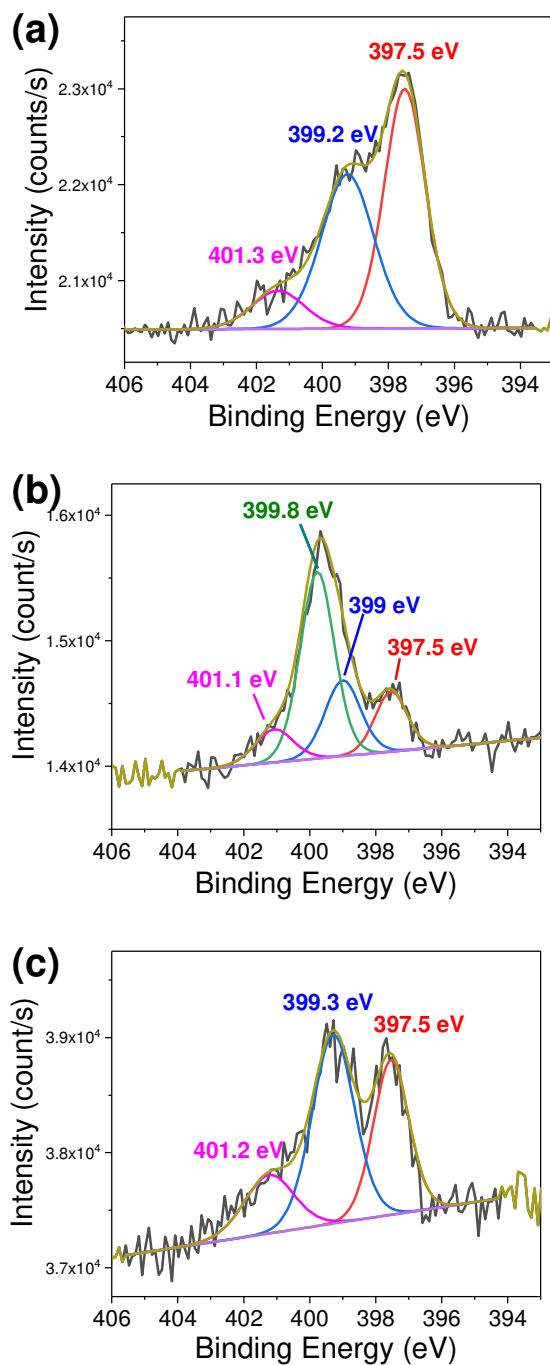


Figure 8. N 1s XPS spectra of Ru NPs prepared by hydrogenation of [Ru(COD)(COT)] in a solution of 1,3,5-trimethylbenzene containing LA and HDA with various molar ratio $A = [LA]/[Ru]$ and $B = [HDA]/[Ru]$: (a) $A = 0$ and $B = 8$; (b) $A = 8$ and $B = 2$; (c) $A = 8$ and $B = 2$ after several washing steps.

3.3 Theoretical calculations and discussion

The structural studies showed that the particles prepared in the absence of LA, or with a small amount of LA in equimolar proportion with HDA ($A=B=1$), crystallized mainly with the *hcp* structure. The surface chemistry studies evidenced amine and N atoms adsorbed at the Ru NP surface and weakly bonded amide in case of mixture of LA and HDA. On the other hand, in the samples prepared with large amount of LA a polymorphism was evidenced with both icosahedral and *hcp* NPs and the surface studies evidenced the presence of carbon monoxide on the surface of the particles, generated *in situ* by the decarbonylation of LA. Since CO was hardly or not observed on the FT-IR spectra of samples for which platelets were the main population (see for example the sample prepared with $A=B=4$ on Fig. 1c or $A=8$ and $B=2$ on Fig. S4b), it is reasonable to assume that the main effect of the presence of CO is to favor the icosahedral structure.

In order to assess if the carbonylation could explain the stabilization of the icosahedral structure, the energies of three model Ru NPs, *hcp*-bipyramid, icosahedron and *fcc*-cuboctahedron, with same number of Ru atoms (147) were calculated as a function of CO surface coverage, temperature and CO partial pressure. So far, the effect of CO adsorption was only considered in the case of the crystallization of *hcp*-Ru NPs.³³ In the present case, our aim is to understand the role of CO adsorption on the stabilization of icosahedral NPs. Even if the syntheses were done under H_2 pressure with concomitant formation of surface hydrides, CO was only considered in the DFT calculations since hydrides are expected to be removed by CO on the surface, given a previous joint theoretical/experimental study about the surface composition of small Ru NPs in equilibrium with syngas.⁵¹ This is related to the very large adsorption energy difference between CO and H_2 (on a Ru_{55} *hcp* model: $E_{ads/CO} \sim -40$ kcal.mol⁻¹ for 1.5 CO/ Ru_{surf} ; $E_{ads/H} \sim -9$ kcal.mol⁻¹ for 1.6 H/ Ru_{surf}).

The relative structural stability of the three bare isomers, *hcp*-bipyramid, icosahedron and *fcc*-cuboctahedron, was first analyzed by comparing their cohesive energies. As expected, the *hcp* isomer was more stable than the icosahedron and *fcc*-cuboctahedron counterparts with cohesive energies per atom $E_{coh} = -5.68$ eV, -5.67 eV and -5.58 eV, respectively. These numbers are very similar to the values reported by Nanba et al.⁴⁵ In terms of total energy, the bare icosahedron and cuboctahedron isomers lie 20 kcal/mol and 329.7 kcal/mol, respectively, above the *hcp* structure. Although this high energy difference found for the cuboctahedron isomer probably precludes the possibility of a stabilization upon carbonylation of its surface, it has been incorporated in the set of structures and energies considered in the thermodynamics model. The resulting predominance diagram is reported in Fig. 9. It is based on the calculation of $\Delta G_{ads}(T, p_{CO})$ for all the isomers and surface coverage values θ considered in this study (see the theoretical part of the experimental section as well as Refs. 51 and 58). The bare *hcp*- Ru_{147} cluster is the most stable isomer at relatively high temperatures and under low pressure of CO. Upon lowering the temperature and for moderate to low CO pressure, the *hcp* core is still the most stable, with a $\theta = 0.25$ CO/ Ru_{surf} coverage value. A striking result is the stabilization of the icosahedral core in the temperature and pressure conditions that favor a surface coverage of at least 0.75 CO/ Ru_{surf} . It is already obvious when comparing the relative energies of the *ico* and *hcp* isomers stabilized with 69 CO ligands (*i.e.* $\theta = 0.75$): the icosahedral NP is more stable than the *hcp* counterpart by 56 kcal.mol⁻¹. The structure, shown in Fig. 9, essentially exhibits edge-bridging CO in agreement with the FT-IR spectra of the Ru particles (see also the comparison between DFT vibrational frequencies and FT-IR data in Ref. 51). A kind of energy decomposition analysis, coupled with a d-band center calculation is proposed in Figure 10 for the 1.00 CO/ $Ru_{surface}$ case. The $Ru_{147}(CO)_{92}$ icosahedral nanocluster is more stable than its *hcp* counterpart by 51.9 kcal.mol⁻¹ (Figure 10a). The inversion of stability between the bare nanoclusters (*hcp* vs. *ico*: -20 kcal.mol⁻¹) and the CO-stabilized clusters can be explained by a stronger adsorption energy of carbon monoxide on the icosahedral metal core: ~ -4055 kcal.mol⁻¹ vs. ~ -3983 kcal.mol⁻¹. Single-point calculations demonstrate that this strong stabilization due to CO adsorption competes both with a still less stable icosahedral Ru_{147} core and

with a steric hindrance between carbon monoxide that is more important in the icosahedral nanocluster (Figure 10b). Indeed, the frozen icosahedral Ru₁₄₇ moiety is less stable than the frozen *hcp* metal core, by 39.4 kcal.mol⁻¹. In the same way, with a +40 kcal.mol⁻¹ relative energy of the 92 frozen CO taken from the icosahedral nanocluster with respect to those taken from the *hcp* one, a spurious steric hindrance of the 92 CO in HCP-Ru₁₄₇(CO)₉₂ can be discarded. The 51.9 kcal.mol⁻¹ relative stability of ICO-Ru₁₄₇(CO)₉₂ seems to originate from a pure electronic effect of the metal core, as shown by the pDOS analysis and by the calculation of the *d*-band center (ϵ_d) reported in Figure 10c. Whereas ϵ_d for the ~55 core metal atoms is almost the same in both compounds (*hcp*: -3.44 eV and *ico*: -3.48 eV), ϵ_d for the surface atoms is significantly closer to the Fermi energy in the icosahedral nanocluster (*hcp*: -2.52 eV and *ico*: -2.43 eV). It makes them more reactive, in line with the stronger adsorption energy calculated in this compound. It is noteworthy that the Ru₁₄₇ *hcp* cluster was designed with steps (see also scheme 1), which atoms exhibit dangling orbitals and are characterized by an intrinsic unstable *d*-band center. Despite the presence of such steps, the overall surface *d*-band center of the *hcp* nanocluster is more stable than that of the icosahedron. In summary, this analysis shows that the ruthenium surface of the icosahedron is more reactive toward CO adsorption. The stabilization of icosahedra is thus related to the electronic properties of the metal moiety and to the CO pressure, that compete with the relative stability of the different crystal packings, intrinsically in favor of a *hcp* metal core.

Note that the DFT calculations have been done on 147 atom clusters while the experimental size of 2 nm corresponds more to clusters of 309 atoms. The calculation time on 309 Ru atoms would have been extremely long because the DFT calculations time scales with N_e^3 with N_e the number of electrons in the clusters. A previous study on the relative stability of metal particles with different shapes and structure did not evidence any energy crossing of the different isomers between 147 and 309 atoms.⁷² We are therefore very confident that the trend obtained with particles of 147 atoms can be transposed to 309 atoms.

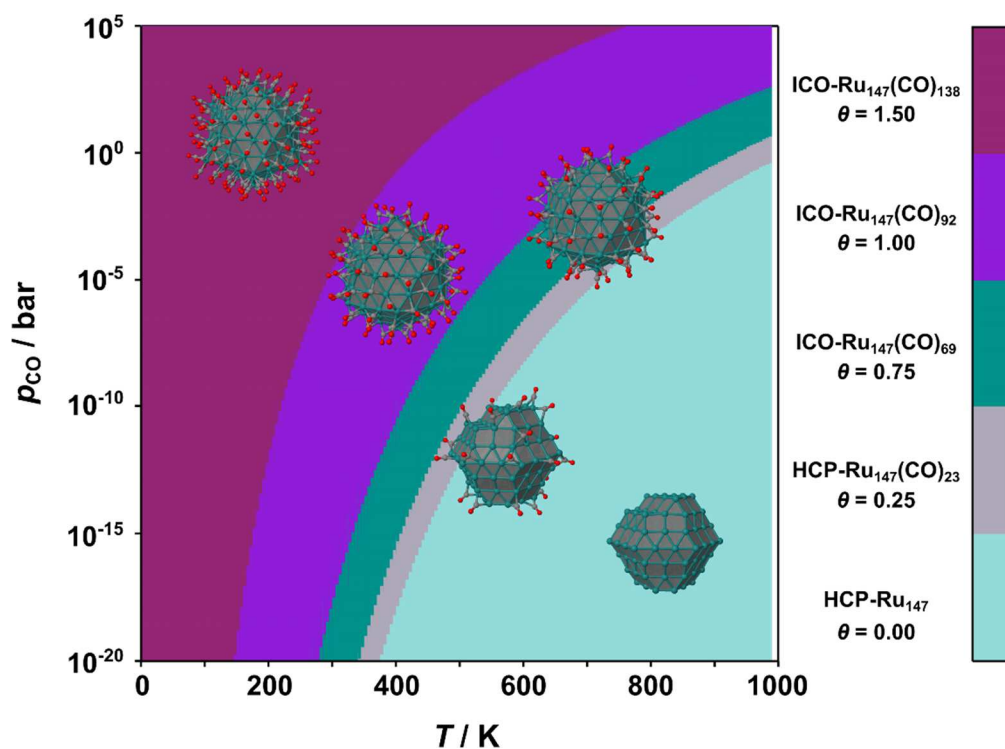


Figure 9. $\Delta G_{\text{ads}}(T, p_{\text{CO}})$ phase diagram for CO adsorption on Ru NPs.

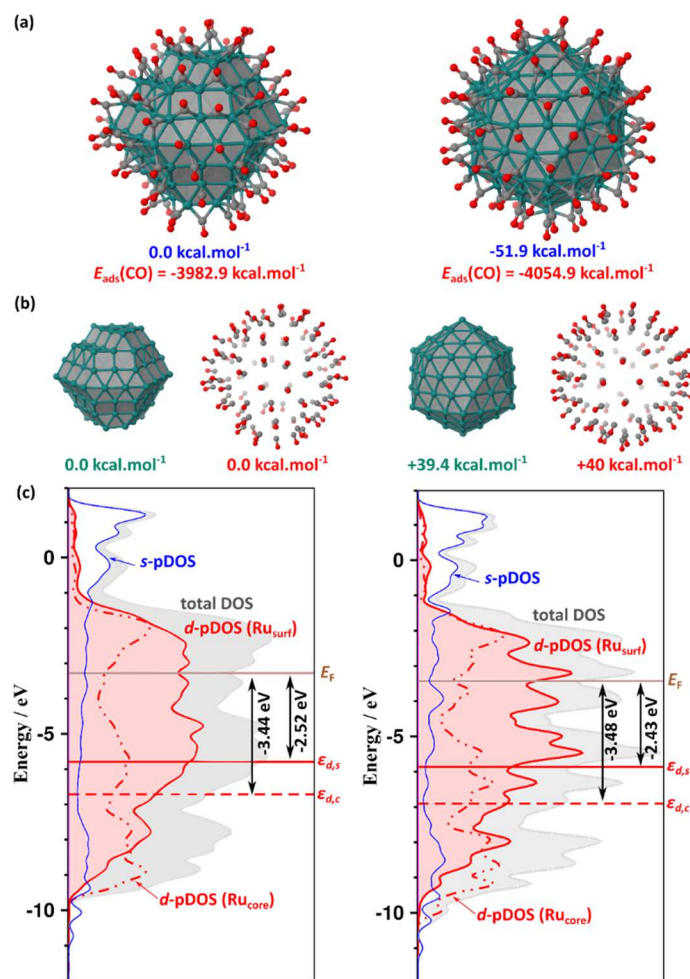


Figure 10. Comparison of energy clues and of projected-density of states (pDOS) for the *hcp*-Ru₁₄₇(CO)₉₂ (left) and of the *ico*-Ru₁₄₇(CO)₉₂ (right) nanoclusters. (a) Geometries and energies relative to the *hcp* nanocluster. CO adsorption energies are also given ($E_{\text{ads}}(\text{CO}) = E(\text{nanocluster}) - E(\text{Ru}_{147}) - 92E(\text{CO})$, where energies are those of the fully optimized species). (b) Relative energies of the Ru₁₄₇ and (CO)₉₂ moieties, after single-point calculations done on frozen geometries, extracted from the optimized Ru₁₄₇(CO)₉₂ structures. (c) projected-density of states (pDOS) and d-band center energies of the surface ($E_{d,s}$) and core ($E_{d,c}$) ruthenium atoms in bare Ru₁₄₇ bare nanoclusters; the Fermi level (E_F) is also shown.

LA is a source of CO that has a strong affinity for the metals and that can orient the crystallization of the ruthenium particles toward the icosahedral structure, as shown by the DFT calculations. However, even in the case of the reaction with a very large excess of LA ($A = 8$) the proportion in number of icosahedral particles and *hcp* three-fold stars is around 50-50 showing a competition between the nucleation of icosahedral and *hcp* seeds. These seeds then grow as platelets or 3-fold stars. A recent unified approach of DFT, Wulff construction and *ab initio* atomistic thermodynamics showed that even if increasing CO surface coverages of Ru NPs favor the flat facets in equilibrium morphology of nanoparticles, the overall shapes of *hcp* Ru NPs covered with CO remain hexagonal bipyramids.⁷³ The formation of ultrathin triangular platelets and 3-fold stars observed in presence of large amount of LA has very likely another origin than only CO adsorption.

LA in the carboxylate form can also be adsorbed on the Ru NP surface. The possible co-adsorption of carboxylates and CO can be evaluated from the comparison of their adsorption energies. DFT calculations of the adsorption of carboxylates and CO on Ru NPs were already published.^{51,52} The CO

adsorption energy on the same Ru NP model varies between $-55 \text{ kcal.mol}^{-1}$ (low CO coverage) and $-37 \text{ kcal.mol}^{-1}$ (very high CO coverage), whereas the dissociative adsorption energy of one molecule of ethanoic acid was found to lie between $-58 \text{ kcal.mol}^{-1}$ on a bare NP and $-30 \text{ kcal.mol}^{-1}$ on a NP stabilized with hydrides and other ethanoates. Given the small differences of the adsorption energies, a competition on the surface between RCOOH and CO could occur. The presence of two particles different in shape and structure may be related to a different stabilization, CO for the icosahedra and long chain carboxylates for the platelets and 3-fold stars. Further theoretical calculations should allow to conclude on this point. In the presence of mixtures of LA/HDA the relative number of icosahedra was limited, likely because of a lower amount of CO generated *in situ*. This can be explained by the formation of amide by condensation of LA and HDA that competes with the LA decomposition limiting the CO *in situ* formation and finally the crystallization of the icosahedral particles. Nevertheless, the large excess of LA still favors the formation of platelets supporting the role of an excess of LA on the stabilization of the (0001) facets of Ru hcp, favoring the growth of ultrathin platelets.

Interestingly, the 3-fold stars were only observed in case of addition of LA alone, i.e. under the same conditions as those favoring the icosahedra. Generally, the formation of stars is explained by two successive nucleation/growth stages resulting from a change in the experimental conditions. At this point of the study, it is difficult to establish clearly why at a given point of the reaction the growth of the $\{10\bar{1}0\}$ lateral facets is inhibited and why a second nucleation occurs at the vertices of the triangles with the growth of the $\{2\bar{1}\bar{1}0\}$ lateral facets.

LA has also a strong effect on the reaction rate. The reaction is fast with pure HDA and is considerably slowed down by adding LA in equimolar proportion or in excess. 4 days at $150 \text{ }^\circ\text{C}$ was necessary for a complete ruthenium NP formation with a large excess of LA while in the absence of carboxylic acid few hours were enough. *In situ* formation of intermediate stable ruthenium complexes in the reaction medium can explain the decreasing nucleation rate and the growth of hcp-Ru seeds into larger platelets and stars. It has already been observed that the thermal decomposition of $[\text{Ru}_3(\text{CO})_{12}]$ under 3 bars of molecular hydrogen in solutions containing mixtures of amine and long-chain acid was strongly slowed down by the increase of the acid/amine ratio.³⁴ Addition of LA in large excess slows down the reaction, limits the number of nuclei and increases the mean size of the particles with the hcp structure. This is only true for the hcp NPs, the icosahedral particles also formed in large excess of LA do not grow beyond a given size. This can be explained by the increasing strain energy with increasing size in the multiply-twinned particles which is commonly observed for Au NPs.

HDA plays very different roles than LA not only in the nucleation and growth steps of the Ru NPs or in the reaction rate but also as reactant. In the presence of pure HDA, or excess of HDA, the nucleation rate is very fast and the growth is limited leading to very small particles with the hcp structure. The C-N activation of HDA produces N atoms adsorbed at the surface of the Ru NPs. At the opposite of CO that has been observed only on the samples containing icosahedra, the surface nitridation has been observed both on NP prepared in excess of amine or with mixtures of amine and acid. This surface nitridation does not seem to have any effect on the Ru NP crystallization, occurring very likely after the crystallization of the Ru NPs.

4. Conclusion

The control of the size and shape of metal NPs synthesized by chemical methods in solution strongly depends on the presence and concentration of ligands added with the metal precursor. Ligands may play several roles throughout the NP formation process. Upon reaction with the initial molecular precursors they can change its nature, thus, modifying the kinetics of the decomposition. They act as surfactant for the stabilization of the nuclei and the final particles. They can also favor the anisotropic

growth by a selective adsorption on some crystallographic facets. In addition, we have shown in this study that they can also be the precursor of small molecules that have a strong interaction with the metal NP surface.

The syntheses of Ru NPs by hydrogenation of [Ru(COD)(COT)] in the presence of long chain carboxylic acid illustrates well these multiple roles. This study demonstrates the high reactivity of the small clusters formed in the initial steps of nanoparticles growth which are able to decarbonylate carboxylic acids to give CO adsorbed at the NP surface or to perform hydrodenitrogenation of terminal amines to give surface nitrides.

Small ruthenium icosahedra, which is a very rare structure for this metal, have been observed in large amount whenever the CO bands are present in the FT-IR spectra of the particles. On the other hand, no influence of surface nitridation on the particle structure was noticed. DFT calculations on different Ru nanoparticles predict that CO could be responsible for the formation of Ru icosahedra. These calculations show that the adsorption of CO on the surface of small Ru seeds favors icosahedral seeds over hcp seeds, and rule out a possible role for the electronic structure or the compactness of the metal icosahedral core. The low CO partial pressure resulting from the decarbonylation of lauric acid can explain the formation of the two types of seeds and eventually two types of particles. Concerning the crystallization of the more classical Ru hcp NPs, the nucleation rate is slowed down in presence of large excess of carboxylic acid favoring the growth of hcp seeds into 2D-platelets and stars.

A future direction of this work is to carry out syntheses of Ru NPs under low CO partial pressure atmosphere to study precisely the conditions favoring the icosahedra. It is expected that the CO partial pressure must be controlled very carefully, a large excess of CO will lead to ruthenium carbonyl clusters and the reaction of an equimolar mixture of CO:H₂ in presence of Ru NPs leads to the formation of carbides.⁷⁴ In addition, the Fischer-Tropsch reaction for which Ru is an active catalyst has to be overlooked when H₂ is also present.³⁴ Such a study is important because it should confirm that CO can orient the crystallization to Ru NPs with unusual shape and structure, thus complementing the DFT results.

Associated contents

Supporting information: Tables summarizing the Ru NP morphology and size obtained for different experimental conditions. Figures showing TEM images, STEM-HAADF images and high-resolution STEM-HAADF images Ru NPs. Local EDS analyses of Ru icosahedra. High-resolution XPS spectra of Ru NPs in the C1s and Ru3d energy range. X-ray photoelectron spectra of Ru NPs. Table summarizing the DFT energies of Ru polyhedra of 147 atoms (HCP, ICO, CUBO). Link to interactive 3D models.

Authors information

Corresponding authors

*E-mail : katerina.soulantika@insa-toulouse.fr

*E-mail : romuald.poteau@univ-tlse3.fr

*E-mail: guillaume.viau@insa-toulouse.fr

Notes

The authors declare no competing financial interest.

Acknowledgement

This work was funded by the French National Research Agency, ANR, in the framework of the TANOPOL project (ANR-15-CE07-0011-01). Teresa Hungria (Plateforme Castaing, Toulouse) is warmly thanked for HAADF-STEM images. We gratefully acknowledge the International Associated Laboratory (LIA)-M²OZART for financial support. High resolution HAADF-STEM images were performed at the Laboratorio de Microscopias Avanzadas, Instituto de Nanociencia de Aragon, Universidad de Zaragoza, Spain. R. A. gratefully acknowledges the support from the Spanish Ministry of Economy and Competitiveness (MINECO) through project MAT2016-79776-P (AEF/FEDER. UE). IdR and RP thank the HPC CALcul en Midi-Pyrénées (CALMIP, OLYMPE machine, grant P0611) for a very generous allocation of computer time on this project.

References

- (1) An, K.; Somorjai, G. A.. *Size and Shape Control of Metal Nanoparticles for Reaction Selectivity in Catalysis. ChemCatChem* **2012**, *4*, 1512-1524.
- (2) Cargnello, M. Colloidal Nanocrystals as Building Blocks for Well-Defined Heterogeneous Catalysts. *Chem. Mater.* **2019**, *31*, 576-596.
- (3) Pal, J.; Pal, T. Faceted metal and metal oxide nanoparticles: design, fabrication and catalysis. *Nanoscale* **2015**, *7*, 14159–14190.
- (4) Zaera, F. Nanostructured materials for applications in heterogeneous catalysis. *Chem. Soc. Rev.* **2013**, *42*, 2746–2762.
- (5) Sharma, N.; Ojha, H.; Bharadwaj, A.; Pathak, D. P., Sharma, R. K. Preparation and catalytic applications of nanomaterials: a review. *RSC Adv.* **2015**, *5*, 53381–53403.
- (6) Xia, Y.; Xiong, Y.; Lim B.; Skrabalak, S. E. Shape-Controlled Synthesis of Metal Nanocrystals: Simple Chemistry Meets Complex Physics? *Angew. Chem., Int. Ed.* **2009**, *48*, 60-103.
- (7) Chen, Y.; Fan, Z.; Zhang, Z.; Niu, W.; Li, C.; Yang, N.; Chen, B.; Zhang, H. Two-Dimensional Metal Nanomaterials: Synthesis, Properties, and Applications. *Chem. Rev.* **2018**, *118*, 6409–6455.
- (8) Pei, Y. ; Huang, L. ; Wang, J.; Han, L. ; Li, S. ; Zhang S. ; Zhang. H. Recent progress in the synthesis and applications of 2D metal nanosheets. *Nanotechnology* **2019**, *30*, 222001.
- (9) Zhao, M.; Xu, L.; Vara, M. ; Elnabawy, A. O. ; Gilroy, K. D. ; Hood, Z. D. ; Zhou, S.; Figueroa-Cosme, L. ; Chi, M.; Mavrikakis, M. ; Xia, Y. *Synthesis of Ru Icosahedral Nanocages with a Face-Centered-Cubic Structure and Evaluation of Their Catalytic Properties. ACS Catal.* **2018**, *8*, 6948–6960.
- (10) Kumar, P. S.; Pastoriza-Santos, I. ; Rodríguez-González, B.; García de Abajo, F. J. ; Liz-Marzán, L. M. High-yield synthesis and optical response of gold nanostars. *Nanotechnology* **2008**, *19*, 015606.
- (11) Liakakos, N. ; Cormary, B. ; Li, X. ; Lecante, P. ; Respaud, M. ; Maron, L. ; Falqui, A. ; Genovese, A. ; Vendier, L. ; Koïnis, S. ; Chaudret, B. ; Soulantica, K. The Big Impact of a Small Detail: Cobalt

Nanocrystal Polymorphism as a Result of Precursor Addition Rate during Stock Solution Preparation. *J. Am. Chem. Soc.* **2012**, *134*, 17922–17931.

(12) Camargo, B. ; Lassagne, B.; Arenal, R.; Gatel, C.; Blon, T. ; Viau, G.; Lacroix, L.-M.; Escoffier, W. Platinum tripods as nanometric frequency multiplexing devices. *Nanoscale* **2017**, *9*, 14635-14640.

(13) Lacroix, L.-M.; Gatel, C.; Arenal, R. ; Garcia, C. ; Lachaize, S.; Blon, T.; Warot-Fonrose, B. ; Snoeck, E. ; Chaudret, B. ; Viau, G. Tuning Complex Shapes in Platinum Nanoparticles: From Cubic Dendrites to Fivefold Stars. *Angew. Chem. Int. Ed.* **2012**, *51*, 4690–4694.

(14) Huang, X. ; Tang, S.; Mu, X. ; Dai, Y. ; Chen, G. ; Zhou, Z.; Ruan, F. ; Yang, Z.; Zheng, N. Freestanding palladium nanosheets with plasmonic and catalytic properties. *Nature Nanotechnol.* **2011**, *6*, 28-32.

(15) Luo, M. ; Yang, Y. ; Sun, Y. ; Qin, Y. ; Li, C. ; Li, Y. ; Li, M. ; Zhang, S. ; Su, D. ; Gu, S. Ultrathin two-dimensional metallic nanocrystals for renewable energy electrocatalysis. *Mater. Today*, **2019**, *23*, 45-56.

(16) Axet, M. R. ; Philippot, K. Catalysis with Colloidal Ruthenium Nanoparticles. *Chem. Rev.* **2020**, *120*, 1085-1145.

(17) Zhao, M.; Xia, Y. Crystal-phase and surface structure engineering of ruthenium nanocrystals. *Nat. Rev. Mater.* **2020**, *5*, 440–459.

(18) Alyami, N. M.; LaGrow, A. P. ; Anjum, D. H.; Guan, C. ; Miao, X.; Sinatra, L.; Yuan, D.-J.; Mohammed, O. F.; Huang, K.-W. ; Bakr, O. M. Synthesis and Characterization of Branched fcc/hcp Ruthenium Nanostructures and Their Catalytic Activity in Ammonia Borane Hydrolysis. *Cryst. Growth Des.* **2018**, *18*, 1509–1516.

(19) Kong, X.; Xu, K.; Zhang, C.; Dai, J.; Oliaee, S. N.; Li, L.; Zeng, X.; Wu, C.; Peng, Z. Free-Standing Two-Dimensional Ru Nanosheets with High Activity toward Water Splitting. *ACS Catal.* **2016**, *6*, 1487–1492.

(20) Bell, T. E. ; Torrente-Murciano, L. H₂ Production via Ammonia Decomposition Using Non-Noble Metal Catalysts: A Review. *Top. Catal.* **2016**, *59*, 1438–1457.

(21) Shu, C. ; Wu, C. ; Long, J. ; Guo, H. ; Dou, S.-X. ; Wang, J. Highly reversible Li-O₂ battery induced by modulating local electronic structure via synergistic interfacial interaction between ruthenium nanoparticles and hierarchically porous carbon. *Nano Energy* **2018**, *57*, 166-175.

(22) Martinez-Prieto, L. M.; Chaudret, B. Organometallic Ruthenium Nanoparticles: Synthesis, Surface Chemistry, and Insights into Ligand Coordination. *Acc. Chem. Res.* **2018**, *51*, 376–384.

(23) Pan, C.; Pelzer, K.; Philippot, K.; Chaudret, B. ; Dassenoy, F.; Lecante, P.; Casanove, M.-J. Ligand-Stabilized Ruthenium Nanoparticles: Synthesis, Organization, and Dynamics. *J. Am. Chem. Soc.* **2001**, *123*, 7584-7593.

(24) Yan, X.; Liu, H. ; Liew, K. Y. *Size control of polymer-stabilized ruthenium nanoparticles by polyol reduction.* *J. Mater. Chem.* **2001**, *11*, 3387–3391.

(25) Viau, G. ; Brayner, R. ; Poul, L. ; Chakroune, N. ; Lacaze, E. ; Fiévet-Vincent, F. ; Fiévet, F. Ruthenium Nanoparticles : Size, Shape and Self-Assemblies. *Chem. Mater.* **2003**, *15*, 486 –494.

(26) Joo, S. H.; Park, J. Y. ; Renzas, J. R. ; Butcher, D. R. ; Huang, W. ; Somorjai, G. A. Size Effect of Ruthenium Nanoparticles in Catalytic Carbon Monoxide Oxidation. *Nano Lett.* **2010**, *10*, 2709–2713.

(27) Tschan, M. J.-L.; Diebolt, O.; van Leeuwen, P. W. N. M. Ruthenium Metal Nanoparticles in Hydrogenation: Influence of Phosphorus-Ligands. *Top. Catal.* **2014**, *57*, 1054–1065.

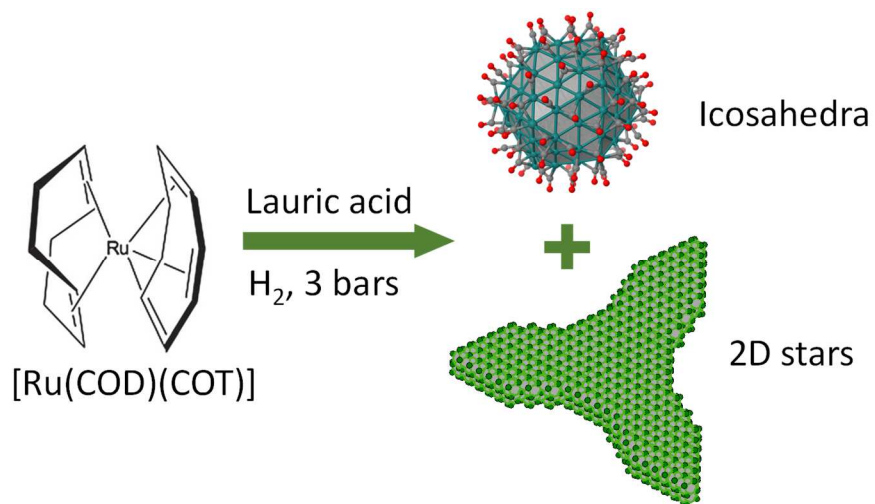
(28) Lee, H.; Habas, S. E.; Kweskin, S. ; Butcher, D. ; Somorjai, G. A.; Yang, P. Morphological Control of Catalytically Active Platinum Nanocrystals. *Angew. Chem. Int. Ed.* **2006**, *45*, 7824 –7828

-
- (29) Wang, C. ; Daimon, H. ; Onodera, T.; Koda, T. ; Sun, S. A General Approach to the Size- and Shape-Controlled Synthesis of Platinum Nanoparticles and Their Catalytic Reduction of Oxygen. *Angew. Chem. Int. Ed.* **2008**, *47*, 3588–3591.
- (30) Bedford, N. ; Dablemont, C. ; Viau, G. ; Chupas, P. ; Petkov, V. 3D Structure of Nanosize Catalysts by High-Energy XRD and RMC Simulations: Study of Ru. *J. Phys. Chem. C* **2007**, *111*, 18214-18219.
- (31) Chen, G. ; Zhang, J. ; Gupta, A. ; Rosei, F. ; Ma, D. Shape-controlled synthesis of ruthenium nanocrystals and their catalytic applications. *New J. Chem.* **2014**, *38*, 1827–1833.
- (32) Watt, J. ; Yu, C. ; Chang, S. L. Y. ; Cheong, S. ; Tilley, R. D. Shape Control from Thermodynamic Growth Conditions: The Case of hcp Ruthenium Hourglass Nanocrystals. *J. Am. Chem. Soc.* **2013**, *135*, 606–609.
- (33) Yin, A.-X. ; Liu, W.-C. ; Ke, J. ; Zhu, W. ; Gu, J. ; Zhang, Y.-W. ; Yan, C.-H. Ru Nanocrystals with Shape-Dependent Surface-Enhanced Raman Spectra and Catalytic Properties: Controlled Synthesis and DFT Calculations. *J. Am. Chem. Soc.* **2012**, *134*, 20479–20489.
- (34) Lignier, P. ; Bellabarba, R. ; Tooze, R. P. ; Su, Z. ; Landon, P. ; Ménard, H. ; Zhou, W. Facile Synthesis of Branched Ruthenium Nanocrystals and Their Use in Catalysis. *Cryst. Growth Des.* **2012**, *12*, 939–942.
- (35) Kusada, K. ; Kobayashi, H. ; Yamamoto, T. ; Matsumura, S.; Sumi, N. ; Sato, K. ; Nagaoka, K. ; Kubota, Y.; Kitagawa, H. Discovery of Face-Centered-Cubic Ruthenium Nanoparticles: Facile Size-Controlled Synthesis Using the Chemical Reduction Method. *J. Am. Chem. Soc.* **2013**, *135*, 5493–5496.
- (36) Mi, J.-L. ; Shen, Y.; Becker, J.; Bremholm, M.; Iversen, B. B. Controlling Allotropism in Ruthenium Nanoparticles: A Pulsed-Flow Supercritical Synthesis and in Situ Synchrotron X-ray Diffraction Study. *J. Phys. Chem. C* **2014**, *118*, 11104–11110.
- (37) Song, C.; Sakata, O. ; Kumara, L. S. R., Kohara, S.; Yang, A.; Kusada, K.; Kobayashi, H.; Kitagawa, H.. Size dependence of structural parameters in fcc and hcp Ru nanoparticles, revealed by Rietveld refinement analysis of high-energy X-ray diffraction data. *Sci. Rep.* **2016**, *6*, 31400.
- (38) Kumara, L. S. R. ; Sakata, O.; Kohara, S.; Yang, A.; Song, C.; Kusada, K.; Kobayashi, H.; Kitagawa, H. Origin of the catalytic activity of face-centered cubic ruthenium nanoparticles determined from an atomic-scale structure. *Phys. Chem. Chem. Phys.* **2016**, *18*, 30622-30629.
- (39) Zhao, M., Chen, Z., Lyu, Z., Hood, Z. D., Xie, M., Vara, M., Chi, M., Xia, Y. Ru octahedral nanocrystals with a face-centered cubic structure, {111} facets, thermal stability up to 400° C, and enhanced catalytic activity. *J. Am. Chem. Soc.* **2019**, *141*, 7028–7036.
- (40) Zheng, Y.; Jiao, Y.; Zhu, Y.; Li, L. H.; Han, Y.; Chen, Y.; Jaroniec, M. ; Qiao, S.-Z. High Electrocatalytic Hydrogen Evolution Activity of an Anomalous Ruthenium Catalyst. *J. Am. Chem. Soc.* **2016**, *138*, 16174-16181.
- (41) Rapps, T. ; Ahlrichs, R. ; Waldt, E.; Kappes, M. M. ; Schooss, D. On the Structures of 55-Atom Transition-Metal Clusters and Their Relationship to the Crystalline Bulk, *Angew. Chem. Int. Ed.* **2013**, *52*, 6102-6105.
- (42) Waldt, E. ; Ahlrichs, R. ; Kappes, M. M. ; Schooss, D. Structures of Medium-Sized Ruthenium Clusters: The Octahedral Motif, *ChemPhysChem* **2014**, *15*, 862-865. D.
- (43) Bumüller, D. ; Hehn, A.-S. ; Waldt, E. ; Ahlrichs, R. ; Kappes, M. M. ; Schooss, Ruthenium Cluster Structure Change Induced by Hydrogen Adsorption: Ru₁₉⁻, *J. Phys. Chem. C* **2016**, *21*, 10645-10652.

-
- (44) Soini, T. M. ; Ma, X. ; Uzengi Aktürk, O. ; Suthirakun, S. ; Genest, A. ; Rösch, N. Extending the cluster scaling technique to ruthenium clusters with hcp structure. *Surf. Sci.* **2016**, *643*, 156-163.
- (45) Nanba, Y. ; Ishimoto, T. ; Koyama, M. Structural Stability of Ruthenium Nanoparticles: A Density Functional Theory Study, *J. Phys. Chem. C* **2017**, *121*, 27445-27452.
- (46) Kresse, G.; Fürthmüller, J. Efficient Iterative Schemes for Ab Initio Total-Energy Calculations Using a Plane-Wave Basis Set. *Phys. Rev. B* **1996**, *54*, 11169–11186.
- (47) Kresse, G.; Fürthmüller, J. Efficiency of Ab Initio Total Energy Calculations for Metals and Semiconductors Using a Plane-Wave Basis Set. *Comput. Mater. Sci.*, **1996**, *6*, 15–50.
- (48) Perdew, J. P.; Burke, K.; Ernzerhof, M. Generalized Gradient Approximation Made Simple. *Phys. Rev. Lett.* **1996**, *77*, 3865–3868.
- (49) Blöchl, P. E. Projector Augmented-Wave Method. *Phys. Rev. B.* **1994**, *50*, 17953–17979.
- (50) Kresse, G.; Joubert, D. From Ultrasoft Pseudopotentials to the Projector Augmented-Wave Method. *Phys. Rev. B.* **1999**, *59*, 1758–1775.
- (51) Cusinato, L. ; Martinez-Prieto, L. M. ; Chaudret, B. ; del Rosal, I. ; Poteau, R. Theoretical characterization of the surface composition of ruthenium nanoparticles in equilibrium with syngas, *Nanoscale* **2016**, *8*, 10974-10992.
- (52) González-Gómez, R. ; Cusinato, L. ; Bijani, C. ; Coppel, Y. ; Lecante, P. ; Amiens, C. ; del Rosal, I. ; Philippot, K. ; Poteau, R. Carboxylic acid-capped ruthenium nanoparticles: experimental and theoretical case study with ethanoic acid, *Nanoscale* **2019**, *11*, 9392-9409.
- (53) Monkhorst, J. D.; Pack, H. J. Special Points for Brillouin-Zone Integrations. *Phys. Rev. B.* **1976**, *13*, 5188–5192.
- (54) Hammer, B.; Nørskov, J. K. Electronic Factors Determining the Reactivity of Metal Surfaces. *Surf. Sci.*, **1995**, *343*, 211–220.
- (55) Maintz, S.; Deringer, V. L.; Tchougréeff, A. L.; Dronskowski, R. LOBSTER: A Tool to Extract Chemical Bonding from Plane-Wave Based DFT. *J. Comp. Chem.* **2016**, *37*, 1030–1035.
- (56) Teo, B. K. ; Sloane, N. J. A. Magic numbers in polygonal and polyhedral clusters, *Inorg. Chem.* **1985**, *24*, 4545-4558.
- (57) Honkala, K. ; Hellman, A. ; Remediakis, I. N. ; Logadottir, A. ; Carlsson, A. ; Dahl, S. ; Christensen, C. H.; Nørskov, J. K. Ammonia Synthesis from First-principles Calculations. *Science* **2005**, *307*, 555-558.
- (58) Cusinato, L.; del Rosal, I.; Poteau, R. Shape, electronic structure and steric effects of organometallic nanocatalysts: relevant tools to improve the synergy between theory and experiments, *Dalton Trans.* **2017**, *46*, 378-395.
- (59) Reuter, K.; Stampfl, C.; Scheffler, M. *Ab initio* atomistic thermodynamics and statistical mechanics of surface properties and functions. in *Handbook of Materials Modeling Series* (Yip, S., Ed.). Springer. **2005**, *1*, 149–194.
- (60) Kittel, C., **2005**. *Introduction to Solid State Physics*. John Wiley & Sons, New York.
- (61) Min, Y. ; Nasrallah, H. ; Poinso, D. ; Lecante, P. ; Tison, Y. ; Martinez, H. ; Roblin, P. ; Falqui, A. ; Poteau, R. ; del Rosal, I. ; Gerber, I. C. ; Hierro, J. -C. ; Axet, M. R. ; Serp, P. 3D Ruthenium Nanoparticle Covalent Assemblies from Polymantane Ligands for Confined Catalysis. *Chem. Mater.* **2020**, *32*, 2365-2378.
- (62) Chin, S. Y. ; Williams, C. T. ; Amiridis, M. D. FTIR Studies of CO Adsorption on Al₂O₃- and SiO₂-Supported Ru Catalysts. *J. Phys. Chem. B* **2006**, *110*, 871-882.

-
- (63) González-Gómez, R. ; Cusinato, L. ; Bijani, C. ; Coppel, Y. ; Lecante, P. ; Amiens, C. ; del Rosal, I. ; Philippot, K. ; Poteau, R. Carboxylic acid-capped ruthenium nanoparticles: experimental and theoretical case study with ethanoic acid. *Nanoscale* **2019**, *11*, 9392-9409.
- (64) Fukasawa, Y., Okuda, T., Shimada, T., Hattori, M., Saito, H. Mechanism of permeability modification in polyethylene foams. *J. Cell. Plast.* **2008**, *44*, 107-123.
- (65) Kaźmierczak, K.; Yi, D.; Jaud, A.; Fazzini, P.-F.; Estrader, M.; Viau, G.; Decorse, P.; Piquemal, J.-Y.; Michel, C.; Besson, M.; Soulantica, K.; Perret, N. Influence of Capping Ligands on the Catalytic Performances of Cobalt Nanoparticles Prepared with the Organometallic Route. *J. Phys. Chem. C* **2021**, *125*, 7711–7720.
- (66) Chakroune, N. ; Viau, G. ; Ammar, S. ; Veautier, D. ; Poul, L. ; Chehimi, M.M. ; Mangeney, C. ; Villain, F. ; Fiévet, F. Acetate and thiol-capped monodisperse ruthenium nanoparticles: XPS, XAS and HRTEM studies. *Langmuir* **2005**, *21*, 6788-6796
- (67) NIST Standard Reference Database 20, Version 4.1. Last Update to Data Content: **2012**. DOI: <http://dx.doi.org/10.18434/T4T88K>. Data compiled and evaluated by Alexander V. Naumkin, Anna Kraut-Vass, Stephen W. Gaarenstroom, and Cedric J. Powell.
- (68) Ogata, Y. ; Aika, K. I. ; Onishi, T. XPS studies of surface nitrogen dissociated from dinitrogen on Raney ruthenium. *Chem. Lett.* **1985**, *14*, 207-210.
- (69) Phadke, P.; Sturm, J. M.; van de Kruijs, R. W.E.; Bijkerk, F. Sputtering and nitridation of transition metal surfaces under low energy, steady state nitrogen ion bombardment. *Appl. Surf. Sci.* **2020**, *505*, 144529.
- (70) Guo, Y.; He, H.; Liu, X.; Chen, Z.; Rioux, R. M.; Janik, M. J.; Savage, P. E. Ring-opening and hydrodenitrogenation of indole under hydrothermal conditions over Ni, Pt, Ru, and Ni-Ru bimetallic catalysts. *Chem. Eng. J.* **2021**, *406*, 126853.
- (71) Rothermel, N.; Limbach, H.-H.; del Rosal, I.; Poteau, R.; Mencia, G.; Chaudret, B.; Buntkowsky, G.; Gutmann, T. Surface reactions of ammonia on ruthenium nanoparticles revealed by 15N and 13C solid-state NMR. *Catal. Sci. Technol.* **2021**, *11*, 4509-4520.
- (72) Chepulskaa, R. V.; Curtarolo, S. Ab Initio Insights on the Shapes of Platinum Nanocatalysts. *ACS Nano* **2011**, *5*, 247–254.
- (73) Zhao, P. ; Cao, Z. ; Liu, X. ; Ren, P. ; Cao, D.-B. ; Xiang, H. ; Jiao, H. ; Yang, Y. ; Li, Y.-W. ; Wen, X.-D. Morphology and Reactivity Evolution of HCP and FCC Ru Nanoparticles under CO Atmosphere. *ACS Catal.* **2019**, *9*, 2768–2776.
- (74) Moraru, I.-T.; Martínez-Prieto, L. M.; Coppel, Y.; Chaudret, B.; Cusinato, L.; del Rosal, I.; Poteau, R. A combined theoretical/experimental study highlighting the formation of carbides on Ru nanoparticles during CO hydrogenation. *Nanoscale* **2021**, *13*, 6902–6915.

Table of Content Graphic



Ruthenium icosahedra and ultrathin platelets: the role of surface chemistry on the nanoparticle structure

Raj Kumar Ramamoorthy,¹ Katerina Soulantica,¹ Iker Del Rosal,¹ Raul Arenal,^{2,3} Philippe Decorse,⁴ Jean-Yves Piquemal,⁴ Bruno Chaudret,¹ Romuald Poteau,¹ Guillaume Viau¹

¹ Université de Toulouse, UMR 5215 INSA, CNRS, UPS, Laboratoire de Physique et Chimie des Nano-Objets, 135 avenue de Rangueil F-31077 Toulouse cedex 4, France

² Laboratorio de microscopias avanzadas (LMA), Instituto de Nanociencia de Aragon (INA), U. Zaragoza, C/ Mariano Esquillor s/n, 50018 Zaragoza, Spain

³ ARAID Foundation, 50018 Zaragoza, Spain

⁴ Université de Paris, ITODYS, CNRS, F-75006 Paris, France

Supplementary information

Table S1. Morphology of Ru nanoparticles

Table S2. Ru nanoparticle sizes

Figure S1-S4. Transmission electron microscopy images of ruthenium nanoparticles

Figure S5. High-resolution HAADF-STEM edgewise image of Ru nanoplatelets

Figure S6. Structural study of *hcp* ruthenium nanoparticles

Figure S7. High-resolution HAADF-STEM image of a Ru with icosahedral structure and comparison with model

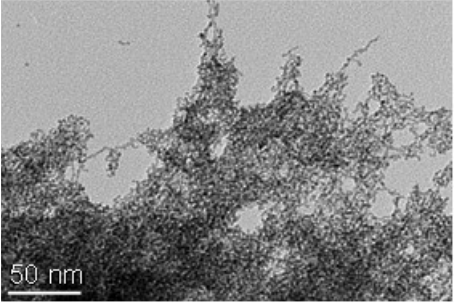
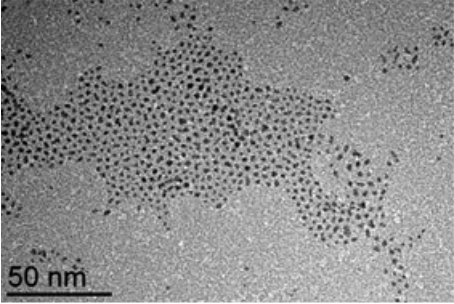
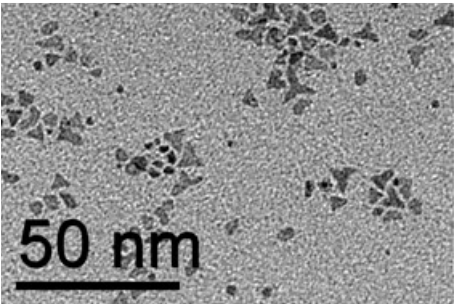
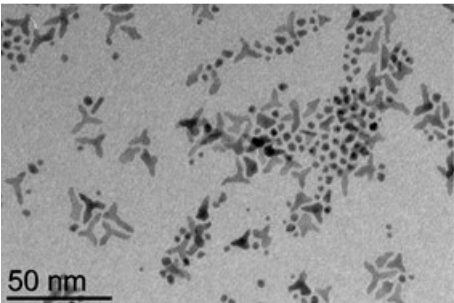
Figure S8. Energy dispersive spectra of Ru nanoparticles

Figure S9. Ru 3d_{5/2}, Ru 3d_{3/2} and C 1s XPS spectra of Ru NPs

Table S3. DFT energies of the isomers

Figure S10. Interactive 3D models

Table S1. Morphology of Ru nanoparticles prepared by hydrogenation at 150 °C of 0.05 M of Ru(COD)(COT) in a solution of 1,3,5-trimethylbenzene containing lauric acid (LA) and hexadecylamine (HDA) with different molar ratios A= [LA]/[Ru] and B= [HDA]/[Ru].

Sample	A	B	Nanoparticle shape	Representative TEM image
1	0	2	Agglomerated NPs	 A transmission electron micrograph showing a dense, interconnected network of dark, irregular nanoparticles. A scale bar in the bottom left corner indicates 50 nm.
2	0	8	Isotropic NPs	 A transmission electron micrograph showing a uniform distribution of small, dark, spherical nanoparticles. A scale bar in the bottom left corner indicates 50 nm.
3	2	0	Isotropic NPs (~50 % in number) and 3-fold stars (~50 % in number)	 A transmission electron micrograph showing a mixture of small, dark, spherical nanoparticles and larger, dark, three-lobed star-shaped structures. A scale bar in the bottom left corner indicates 50 nm.
4	8	0		 A transmission electron micrograph showing a mixture of small, dark, spherical nanoparticles and larger, dark, three-lobed star-shaped structures. A scale bar in the bottom left corner indicates 50 nm.

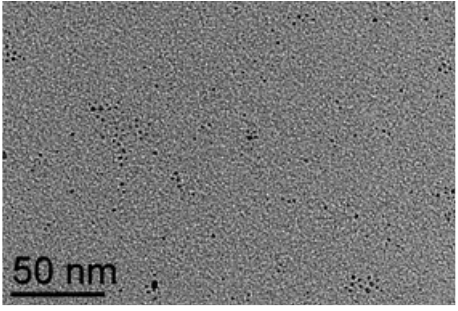
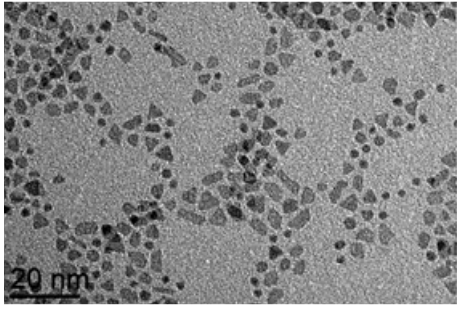
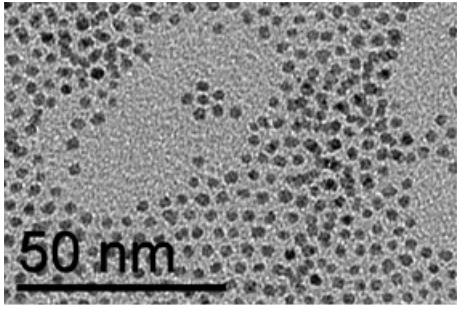
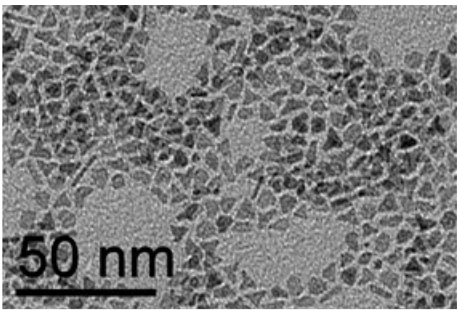
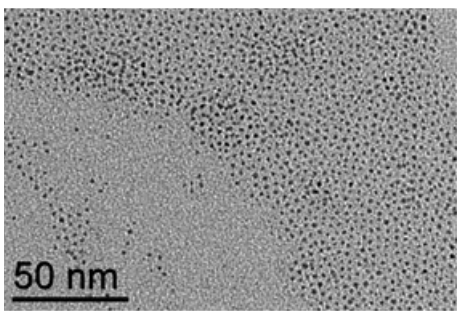
5	1	1	Isotropic NPs	
6	2	2	Isotropic NPs and faceted platelets	
7	4	4		
8	8	8	Isotropic NPs and small platelets	
9	4	1	Platelets with triangular shape + minor population of isotropic NPs (~10 % in number)	
10	8	2		
11	1	4	Isotropic NPs	
12	1	8		

Table S2. Mean size (d_m) and standard deviation of the size distribution (σ) of Ru nanoparticle size prepared with different molar ratio A= [LA]/[Ru] and B= [HDA]/[Ru]

Sample	A	B	Isotropic NPs	Platelets and Stars
2	0	8	$d_m = 2 \text{ nm}$ ($\sigma = 0.5 \text{ nm}$) $\sigma/d_m = 25 \%$	-
3	2	0	$d_m = 2.2 \text{ nm}$ ($\sigma = 0.5 \text{ nm}$) $\sigma/d_m = 23 \%$	$d_m = 8 \text{ nm}$ ($\sigma = 0.8 \text{ nm}$) $\sigma/d_m = 10 \%$
4	8	0	$d_m = 3.5 \text{ nm}$ ($\sigma = 0.7 \text{ nm}$) $\sigma/d_m = 20 \%$	$d_m = 12 \text{ nm}$ ($\sigma = 2 \text{ nm}$) $\sigma/d_m = 17 \%$
5	1	1	$d_m = 1.5 \text{ nm}$ ($\sigma = 0.3 \text{ nm}$) $\sigma/d_m = 20 \%$	-
6	2	2	$d_m = 1.6 \text{ nm}$ ($\sigma = 0.3 \text{ nm}$) $\sigma/d_m = 19 \%$	$d_m = 3.7 \text{ nm}$ ($\sigma = 0.4 \text{ nm}$) $\sigma/d_m = 11 \%$
7	4	4	$d_m = 1.8 \text{ nm}$ ($\sigma = 0.3 \text{ nm}$) $\sigma/d_m = 17 \%$	$d_m = 3.7 \text{ nm}$ ($\sigma = 0.6 \text{ nm}$) $\sigma/d_m = 16 \%$
8	8	8	$d_m = 2.6 \text{ nm}$ ($\sigma = 0.4 \text{ nm}$) $\sigma/d_m = 15 \%$	
9	4	1	$d_m = 2.0 \text{ nm}$ ($\sigma = 0.2 \text{ nm}$) $\sigma/d_m = 10 \%$	$d_m = 4.2 \text{ nm}$ ($\sigma = 0.6 \text{ nm}$) $\sigma/d_m = 14 \%$
10	8	2	$d_m = 2.4 \text{ nm}$ ($\sigma = 0.3 \text{ nm}$) $\sigma/d_m = 13 \%$	$d_m = 7 \text{ nm}$ ($\sigma = 0.9 \text{ nm}$) $\sigma/d_m = 13 \%$
11	1	4	$d_m = 1.5 \text{ nm}$ ($\sigma = 0.2 \text{ nm}$) $\sigma/d_m = 14 \%$	-
12	1	8	$d_m = 1.6 \text{ nm}$ ($\sigma = 0.3 \text{ nm}$) $\sigma/d_m = 20 \%$	-

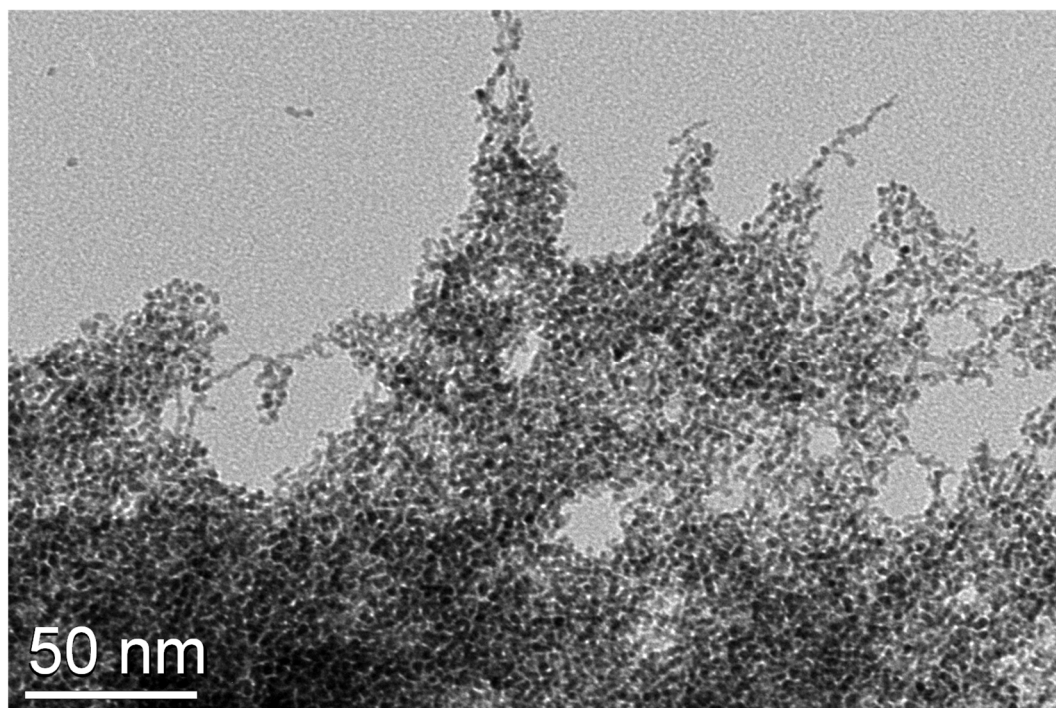


Figure S1. Transmission electron microscopy images of ruthenium nanoparticles prepared by hydrogenation of 0.05 M of [Ru(COD)(COT)] in a solution of 1,3,5-trimethylbenzene containing hexadecylamine with the molar ratio $B = [\text{amine}]/[\text{Ru}] = 2$ and $A = 0$ (reaction in absence of lauric acid).

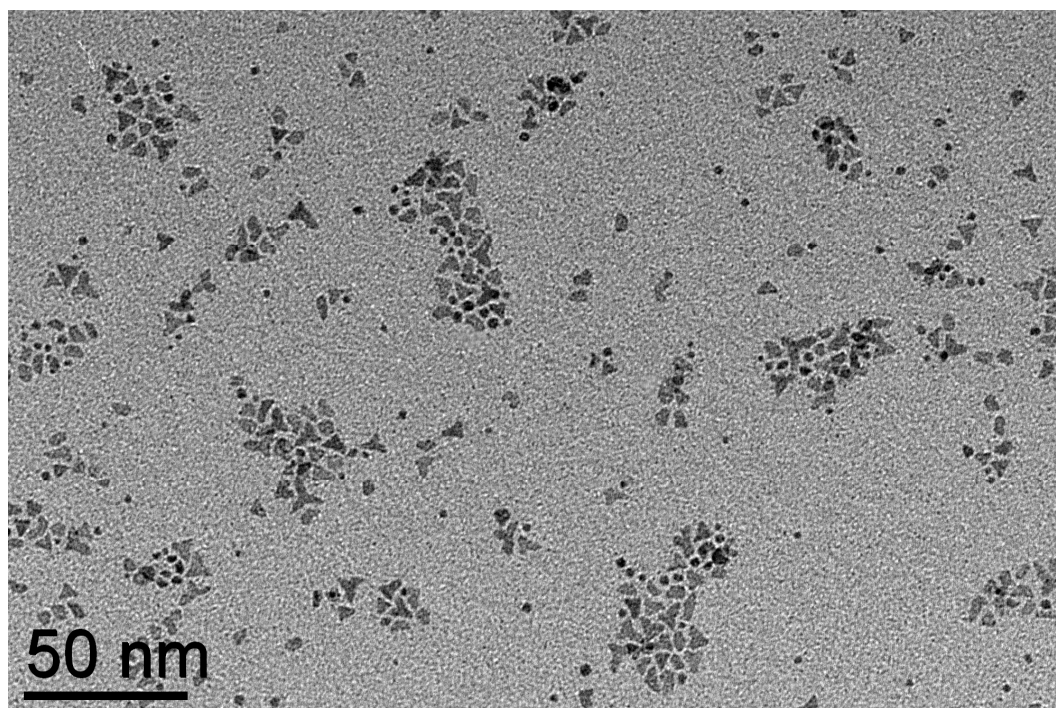


Figure S2. Transmission electron microscopy images of ruthenium nanoparticles prepared by hydrogenation of 0.05 M of [Ru(COD)(COT)] in a solution of 1,3,5-trimethylbenzene containing lauric acid with the molar ratio $A = [\text{acid}]/[\text{Ru}] = 2$ and $B = 0$ (reaction in absence of hexadecylamine).

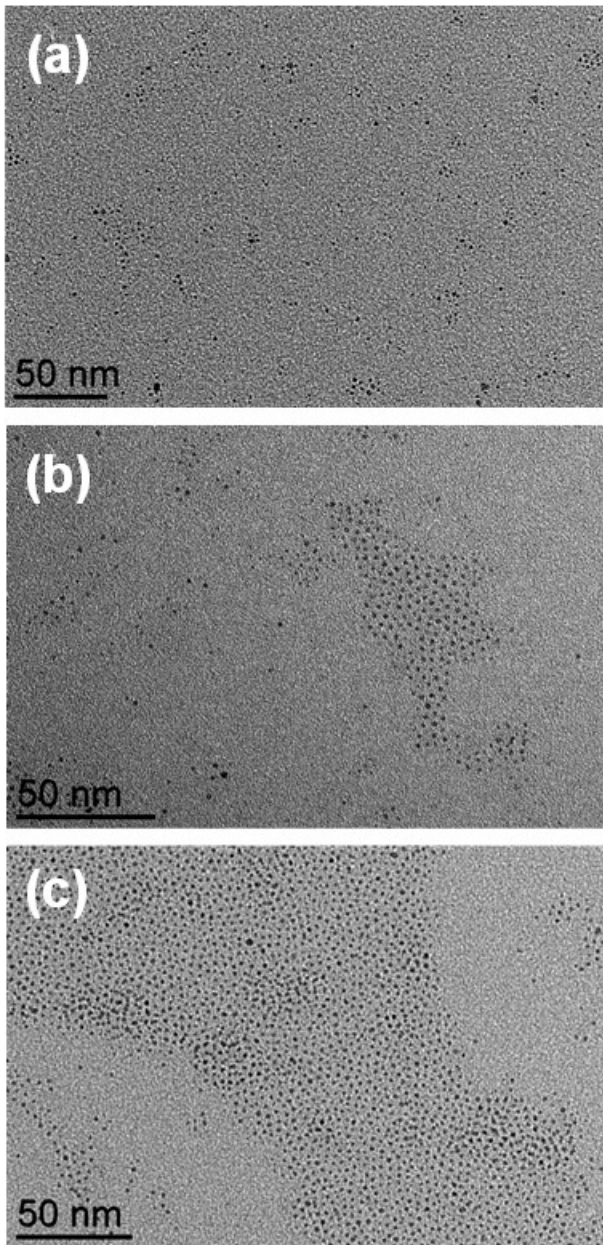


Figure S3. Transmission electron microscopy images of ruthenium nanoparticles prepared by hydrogenation of 0.05 M of $[\text{Ru}(\text{COD})(\text{COT})]$ in a solution of 1,3,5-trimethylbenzene containing lauric acid and hexadecylamine with various molar ratios $A = [\text{acid}]/[\text{Ru}]$ and $B = [\text{amine}]/[\text{Ru}]$: (a) $A = 1, B = 1$ ($d_m = 1.5$ nm); (b) $A = 1, B = 4$ ($d_m = 1.5$ nm); (c) $A = 1, B = 8$ ($d_m = 1.6$ nm).

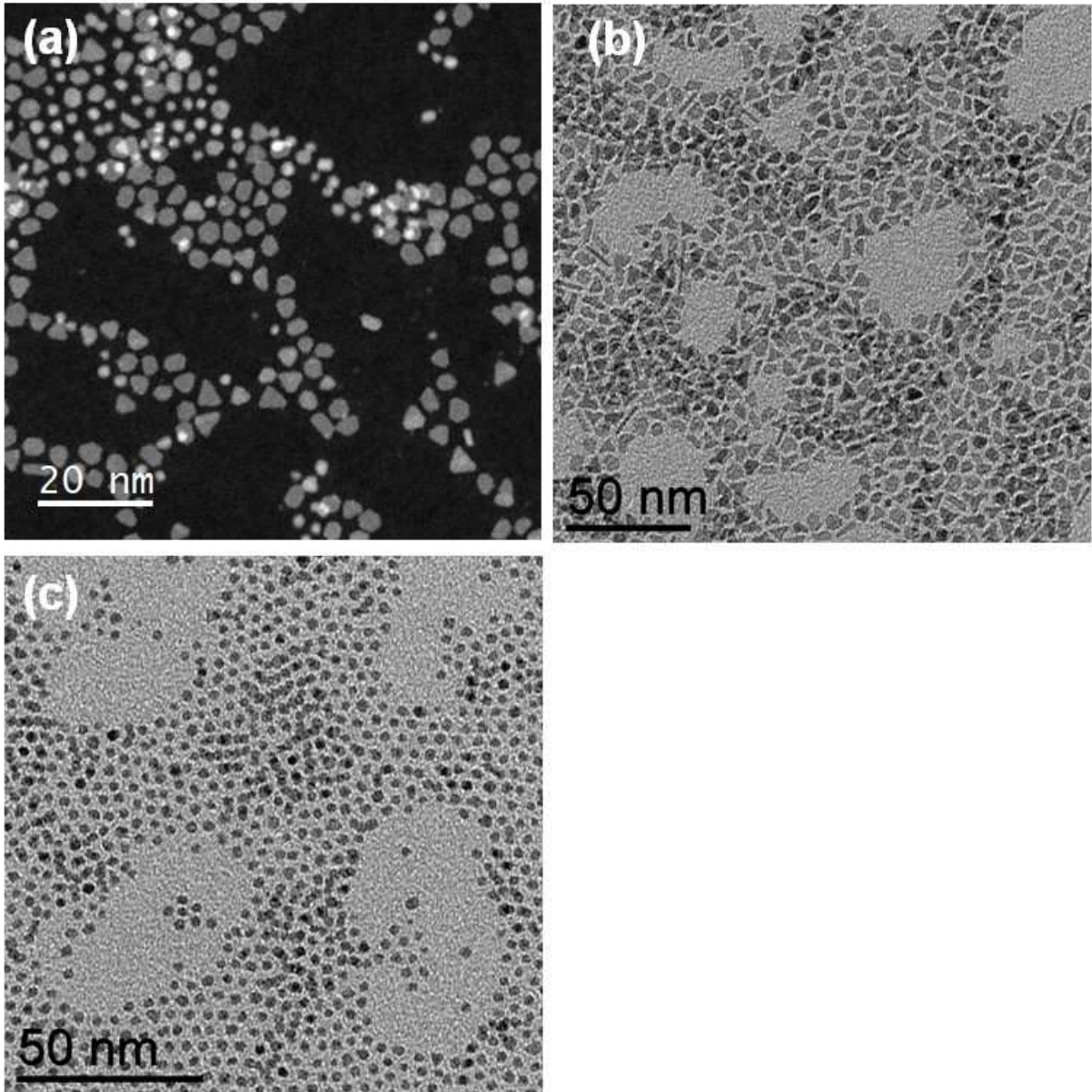


Figure S4. Transmission electron microscopy images of ruthenium nanoparticles prepared by hydrogenation of 0.05 M of $[\text{Ru}(\text{COD})(\text{COT})]$ in a solution of 1,3,5-trimethylbenzene containing lauric acid and hexadecylamine with various molar ratios $A = [\text{acid}]/[\text{Ru}]$ and $B = [\text{amine}]/[\text{Ru}]$: (a) $A = 4$ and $B = 1$; (b) $A = 8$ and $B = 2$; (c) $A = B = 8$.

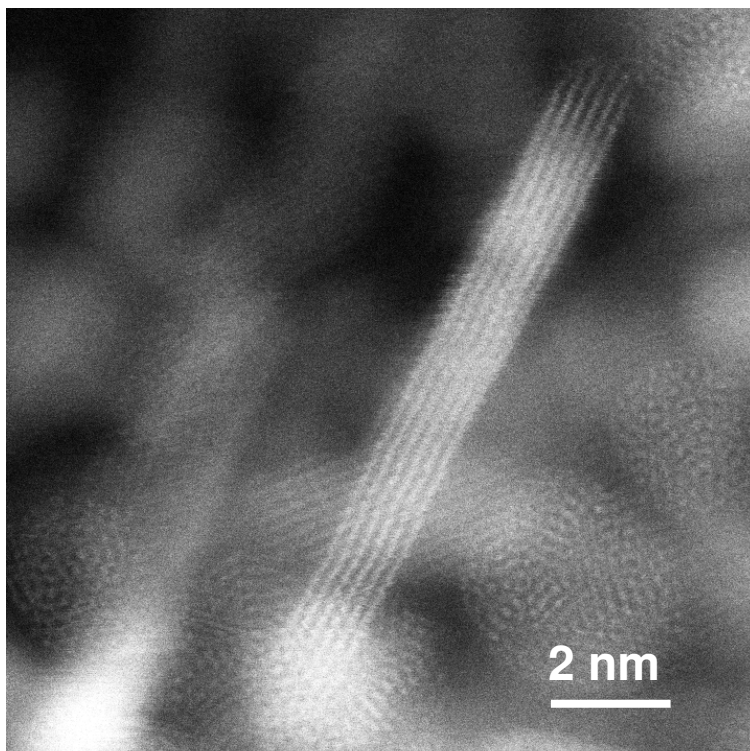


Figure S5. High-resolution HAADF-STEM edgewise image of Ru nanoplatelets prepared with the molar ratios $A = 8$ and $B = 0$, that consists in the stacking of six atomic (0002) Ru layers with a thickness of 10.7-10.8 Å.

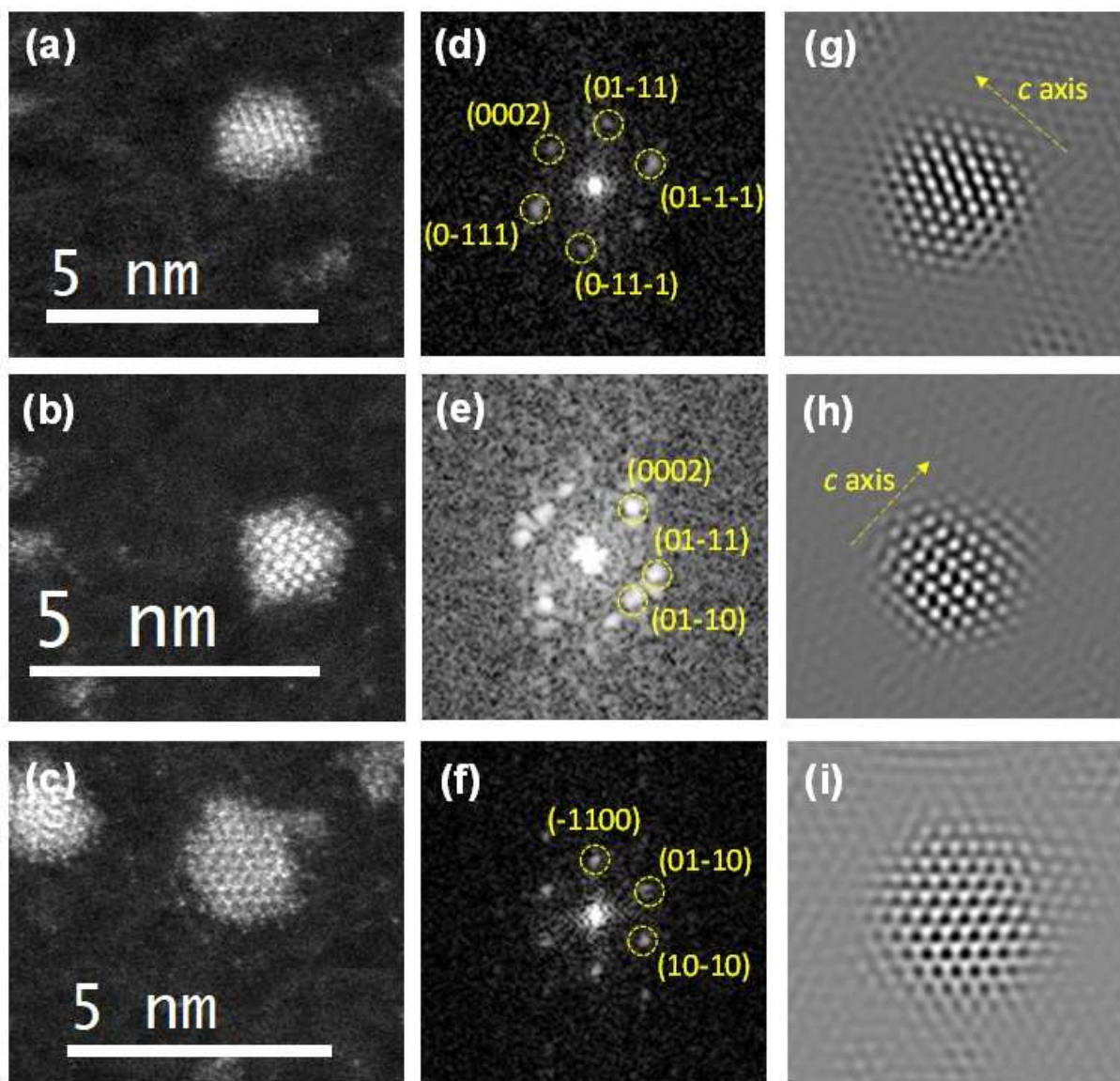


Figure S6. Structural study of ruthenium nanoparticles prepared by hydrogenation of Ru(COD)(COT) in a solution of 1,3,5-trimethylbenzene containing an equimolar amount of lauric acid and hexadecylamine, $A = B = 1$, with $A = [\text{acid}]/[\text{Ru}]$ and $B = [\text{amine}]/[\text{Ru}]$. (a-c) Transmission electron microscopy images (particle size = 2 nm); (d-f) Corresponding Fast Fourier transform images; (g-i) Corresponding filtered Fourier transform images. Nanoparticles (a) and (b) are indexed as *hcp* particles in the $[11\bar{2}0]$ zone axis. Nanoparticle (c) is indexed as *hcp* particles in the $[0001]$ zone axis

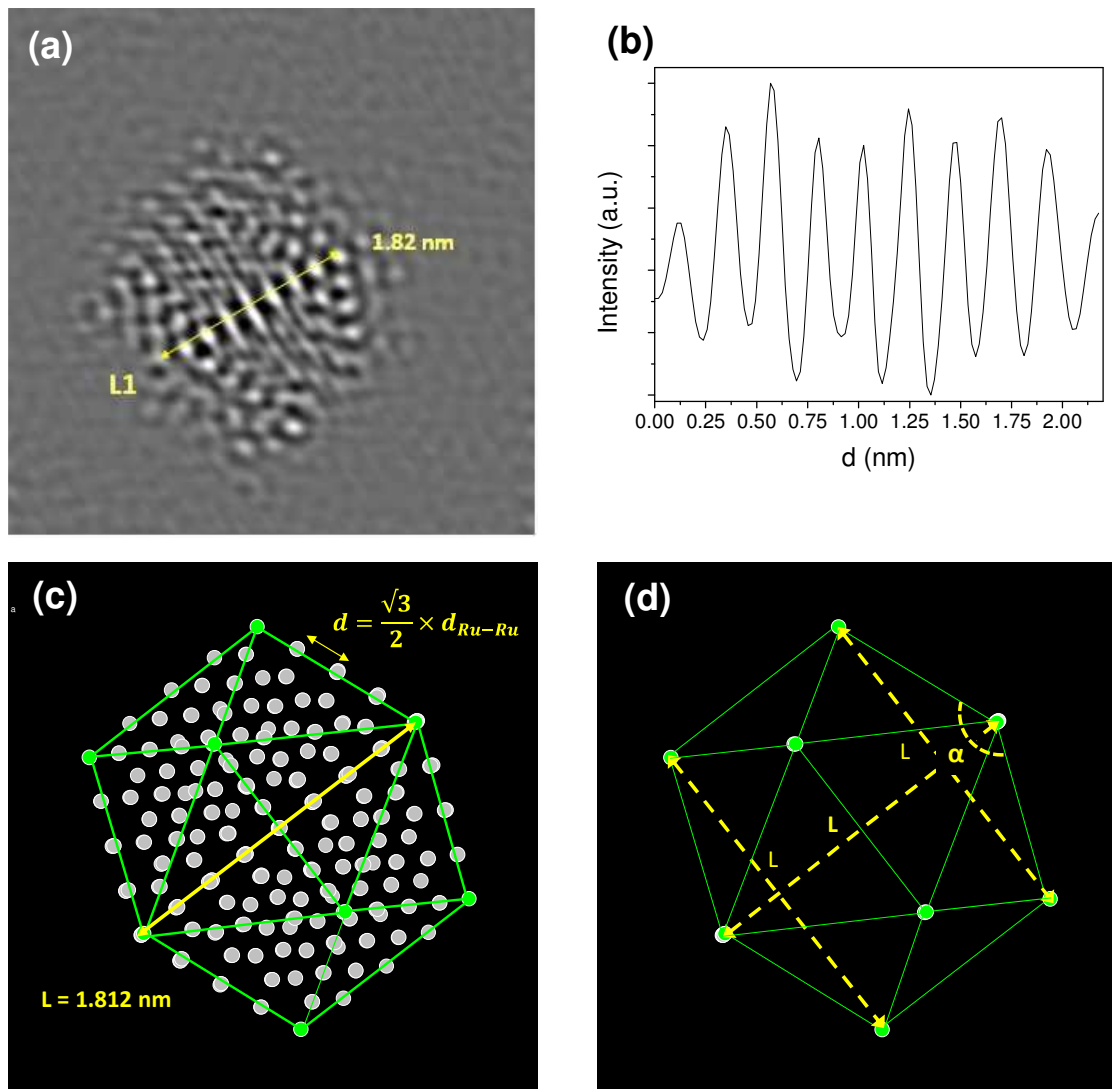


Figure S7. (a) High resolution HAADF-STEM image of a Ru icosahedron viewed along a 2-fold axis ; (b) Intensity profile showing that the interatomic distance measured along the line L1 of figure (a) is constant and equal to 2.27 Å ; (c) Model of a 309 atoms Ru icosahedron viewed along a 2-fold axis (the green atoms correspond to vertices and the green lines to the edges of the icosahedron); in this orientation the distance measured in the projection plane between two opposite vertices of two adjacent facets is 1.812 nm, similar to the experimental measurements; (d) Projection of the icosahedron edges along the 2-fold axis with L the distance between two opposite vertices of two adjacent facets and α the dihedral angle between two adjacent facets. The distance L corresponds to the projection of eight times the distance $= \frac{\sqrt{3}}{2} \times d_{Ru-Ru}$, with d_{Ru-Ru} the mean distance between surface atoms. Thus, the relationship between the distance L and d_{Ru-Ru} is given by:

$$L = \frac{\sqrt{3}}{2} \times d_{Ru-Ru} \times \sin\left(\frac{\alpha}{2}\right)$$

With the experimental values $L = 1.82$ nm and $\alpha = 136.6^\circ$, the mean surface interatomic distance d_{Ru-Ru} is found equal to 2.827 Å, slightly longer than in the *hcp* Ru (2.705 Å).

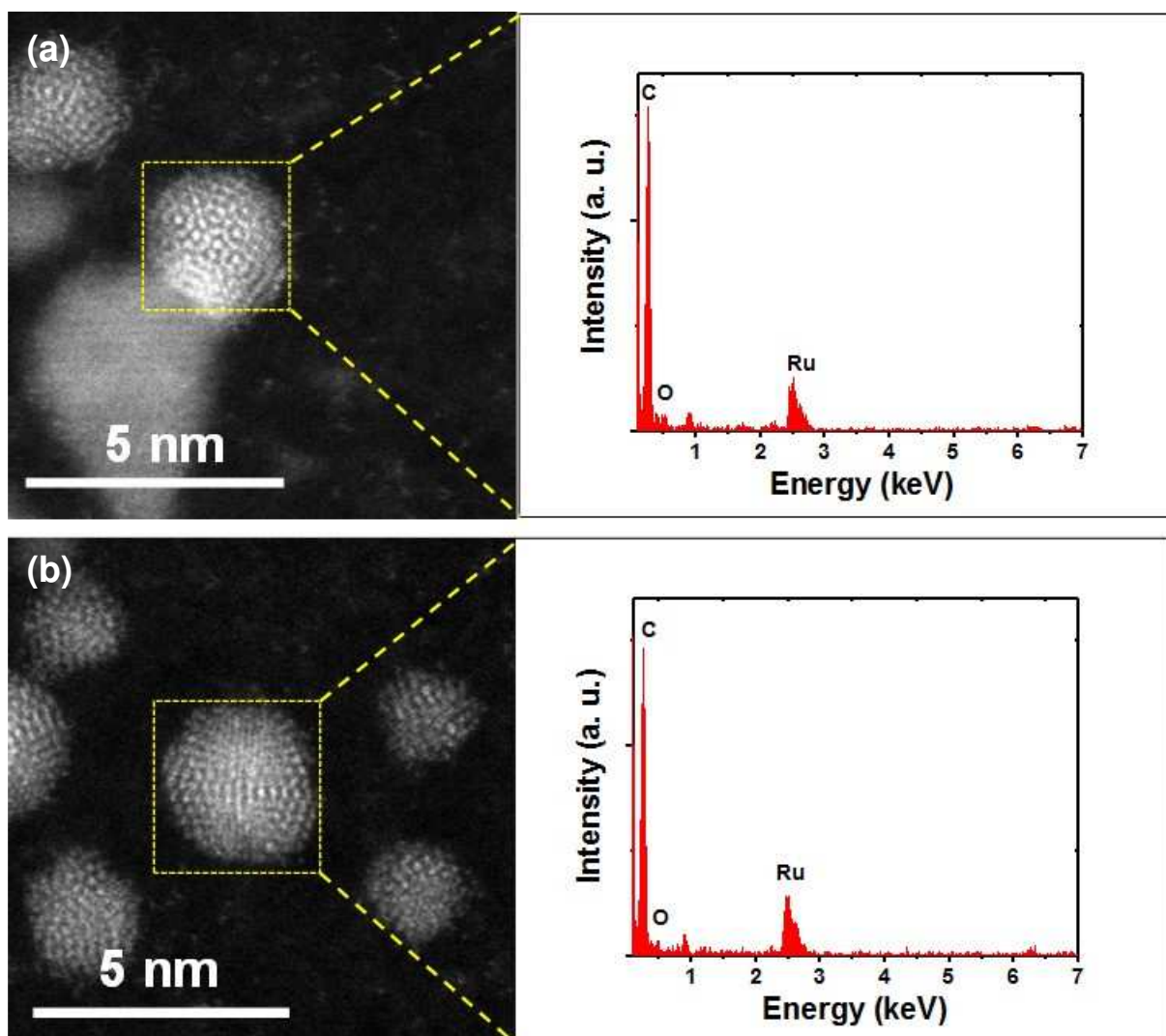


Figure S8. Energy dispersive spectra of Ru nanoparticles prepared by hydrogenation of Ru(COD)(COT) in a solution of 1,3,5-trimethylbenzene containing lauric acid with the molar ratios $A = [\text{acid}]/[\text{Ru}] = 2$ and $B = [\text{amine}]/[\text{Ru}] = 0$: (a) icosahedron viewed along an axis slightly tilted with respect to a 5-fold axis; (b) icosahedron viewed along a 2-fold axis.

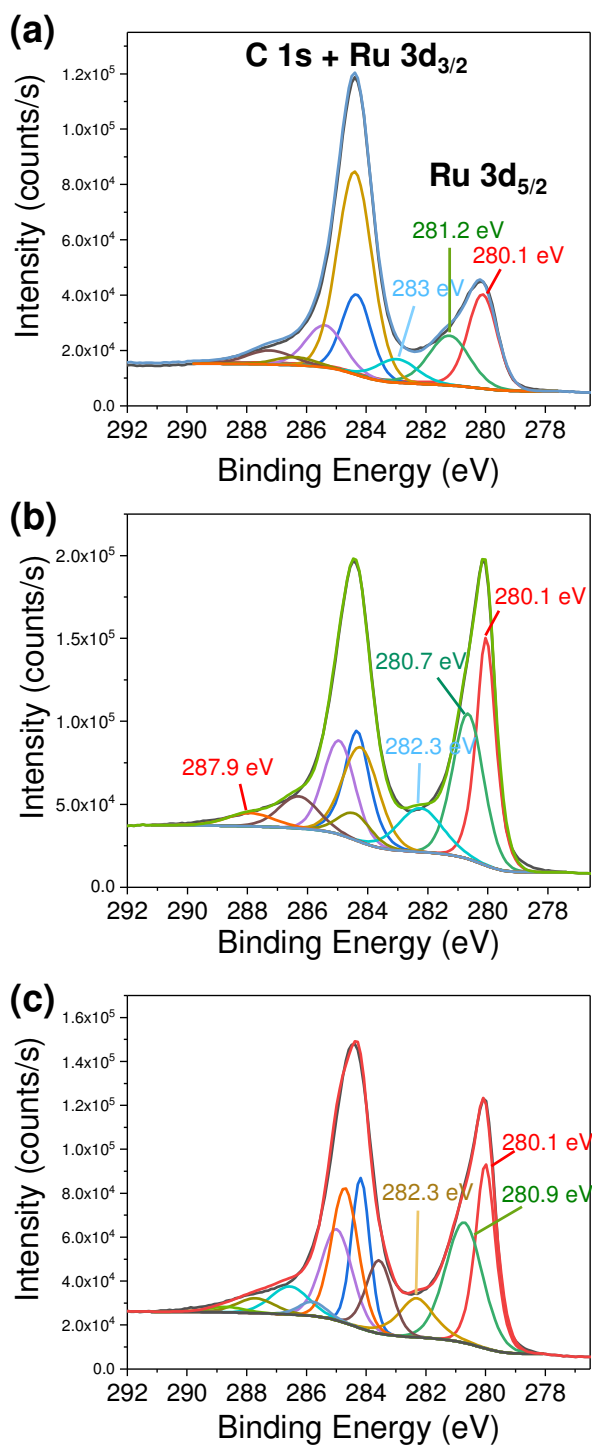


Figure S9. Ru 3d_{5/2}, Ru 3d_{3/2} and C 1s XPS spectra of Ru NPs prepared by hydrogenation of Ru(COD)(COT) in a solution of 1,3,5-trimethylbenzene containing lauric acid and hexadecylamine with various molar ratios A = [acid]/[Ru] and B = [amine]/[Ru]: (a) A = 0 and B = 8 ; (b) A = 8 and B = 2 ; (c) A = 8 and B = 0. The main Ru 3d_{5/2} peak centered at 280.1 eV corresponds to zerovalent Ru atoms. The Ru 3d_{5/2} peaks at higher energies indicated on the figure correspond to surface Ru atoms involved in chemical bonds with surface ligands. The strong C 1s peak at 284.7 eV correspond to the long aliphatic chains of the ligands and the C 1s peak at high energy (287.9 eV) appearing in the figures (b) and (c) corresponds to the C atoms of either the amide or the carboxylic acid groups.

Table S3. DFT energies of Ru polyhedra of 147 atoms (size ~1.4 nm), *hcp* bipyramid (HCP), icosahedron (ICO) and *fcc* cuboctahedron (CUBO).

	EDFT / eV	nRu	nCO	23.06 (ev > kcal/mol)			surface energy		
				Ecoh/N		Relative energies	eV / Å ²		
				kcal/mol	eV	kcal/mol	ref=hcp bulk		
Ru atomic	-2.476549	1	0						
Ru hcp bulk	-6.670000								
CO	-14.775235	0	1						
Ru147-CUBO	-1184.600633	590.4	147	0	-128.7	-5.582	329.7	0.271	6.2
Ru147-ICO	-1198.021674	565.2	147	0	-130.8	-5.673	20.2	0.259	6.0
Ru147-HCP	-1198.896185	586.7	147	0	-131.0	-5.679	0.0	0.248	5.7
				Eads/CO	Relative energies/ Ru atom				
				kcal/mol	kcal/mol				
Ru147-ICO-POSCAR-G25COmu	-1587.560746	147	23	-49.8	0.0		a		
Ru147-ICO-POSCAR-G75COmu	-2357.390041	147	69	-46.7	0.0		b		
Ru147-ICO-POSCAR-G100COmu	-2733.185535	147	92	-44.1	0.0		c		
Ru147-ICO-POSCAR-G100COtop	-2726.312626	147	92	-42.4	1.1				
Ru147-ICO-POSCAR-G150COmu	-3449.146993	147	138	-35.4	0.0		d		
Ru147-CUBO-POSCAR-G25COmu	-1575.552372	147	23	-51.3	1.9		ref=a		
Ru147-CUBO-POSCAR-G75COmu	-2347.450433	147	69	-43.4	1.6		ref=b		
Ru147-CUBO-POSCAR-G100COmu	-2725.645459	147	92	-42.2	1.2		ref=c		
Ru147-CUBO-POSCAR-G150COmu	-3442.381650	147	138	-34.3	1.1		ref=d		
Ru147-HCP-G25COmu	-1588.140030	147	23	-49.5	-0.1		ref=a		
Ru147-HCP-G75COmu	-2354.971902	147	69	-45.6	0.4		ref=b		
Ru147-HCP-G100COmu	-2730.935116	147	92	-43.3	0.4		ref=c		
Ru147-HCP-G150COmu	-3415.538642	147	138	-29.7	5.3		ref=d		

virtual Chemistry 3D

More informations on Wikipedia about [platonic](#), [archimedean](#) and [catalan](#) solids.

Figure S10. Several 3D models can be found at http://vchem3d.univ-tlse3.fr/vM_NanoCrystals.html. Selection of the “FF HRTEM-like model” button gives access to projections as those reported in Figs. 6 and S7.